



**HAL**  
open science

## High-speed infrared thermography for in-situ damage monitoring during impact test

Julien Berthe, Salim Chaibi, Gérald Portemont, Pascal Paulmier, Frédéric Laurin, Christophe Bouvet

► **To cite this version:**

Julien Berthe, Salim Chaibi, Gérald Portemont, Pascal Paulmier, Frédéric Laurin, et al.. High-speed infrared thermography for in-situ damage monitoring during impact test. *Composite Structures*, 2023, 314, pp.116934. 10.1016/j.compstruct.2023.116934 . hal-04053467

**HAL Id: hal-04053467**

**<https://hal.science/hal-04053467>**

Submitted on 31 Mar 2023

**HAL** is a multi-disciplinary open access archive for the deposit and dissemination of scientific research documents, whether they are published or not. The documents may come from teaching and research institutions in France or abroad, or from public or private research centers.

L'archive ouverte pluridisciplinaire **HAL**, est destinée au dépôt et à la diffusion de documents scientifiques de niveau recherche, publiés ou non, émanant des établissements d'enseignement et de recherche français ou étrangers, des laboratoires publics ou privés.

# High-speed infrared thermography for in-situ damage monitoring during impact test

Julien Berthe<sup>a,\*</sup>, Salim Chaibi<sup>b</sup>, Gérald Portemont<sup>a</sup>, Pascal Paulmier<sup>b</sup>, Frédéric Laurin<sup>b</sup> and Christophe Bouvet<sup>c</sup>

<sup>a</sup>DMAS, ONERA, F-59014 Lille - FRANCE

<sup>b</sup>DMAS, ONERA, Université Paris Saclay, F-92322 Châtillon - FRANCE

<sup>c</sup>Université de Toulouse, Institut Clément Ader, ISAE-SUPAERO – UPS – IMT Mines Albi – INSA – CNRS – 10 av. E. Belin, 31055 Toulouse Cedex 4, France

---

## ARTICLE INFO

### Keywords:

Infrared thermography  
Impact tests  
Damage  
Composite materials

## ABSTRACT

The impact damage tolerance remains for laminated composite materials one of the critical step in the design of aeronautical structures. Due to couplings between the different involved damage mechanisms (transverse cracks, delamination, fibre failure), the determination of the damage scenarios is still very challenging considering only post-mortem controls, such as C-Scan or more recently CT-Scan. Therefore, the present study is dedicated to the real time measurement of the evolution of different damage mechanisms during low velocity / low energy impact tests using high-speed infrared thermography. Impact tests at different energy levels were conducted on a T700GC/M21 quasi-isotropic laminate in order to demonstrate for different damage scenarios of increasing complexity the contribution of this measurement technique and to extract valuable information in order to validate simulation. Various post-mortem observation techniques (SEM, C-scan and X-ray tomography) are used in this study to validate and/or determine the chronology of the various damage events identified with infrared thermography measurements. Finally the projected damaged areas have been estimated with IR-thermography at the end of impact tests, based on methodologies available in the literature, and compared with other classical post-mortem measurement methods. This comparison highlights that the assessment of the extent of damage by IR thermography tends to overestimate the extent of damage.

---

## 1. Introduction

With the development of high-performance materials such as composites, significant weight savings in primary aeronautical structures are enabled. However, to pass the certification, aircraft manufacturers must prove that composite structures are as safe as metallic structures. Components made from laminated composite materials have good in-plane mechanical performances but are poorly damage tolerant, especially after an impact. It represents therefore a critical sizing case for aircraft manufacturers. Thus, to help the substantiation, regulation authorities classified the impact severity into five categories (Hempe, 2010). Category I concerns the impact damages created after a low-velocity/low-energy impact (LVI/LEI). It is actually the most critical category as the generated impact damages decrease the residual compressive strength and are difficultly detectable during the scheduled ground operations (Bouvet and Rivallant, 2023). LVI/LEI have been widely studied by academics, experimentally at the first point (Abrate (1998); Davies and Olsson (2004); Olsson (2000); Cantwell and Morton (1989); Kwon and Sankar (1993)) to understand the physical responses of the material when subjected to an impact. These studies have enabled the development of analytical models to predict, among other things, contact time and resistance to delamination. Additionally, post-mortem inspections of impacted samples using ultrasonic scans (Aymerich and Meili, 2000; Wronkiewicz-Katunin, Katunin and Dragan, 2019) or X-rays (Hawyes, Curtis and Soutis, 2001) have enriched the understanding of the damage mechanisms but provide only a damage footprint. These last decades, impact damage assessments have been performed using CT scans, and a 3D volume of the sample is obtained providing a deep understanding of the damage extend and couplings between damage mechanisms (Bull, Helfen, Sinclair, Spearing and Baumbach, 2013; Ellison, 2020). However, the resolution is dependent on the sample's size and when samples are highly warped, it becomes difficult

---

\*Corresponding author

 [julien.berthe@onera.fr](mailto:julien.berthe@onera.fr) (J. Berthe)

 [www.onera.fr](http://www.onera.fr) (J. Berthe)

ORCID(s): 0000-0001-7511-2910 (J. Berthe)

to analyze. Numerically, several studies have developed impact models in order to reconstitute the damage scenario occurring during impact (Chaibi, 2022; De Moura and Gonçalves, 2004; Allix and Blanchard, 2006; Li, Reid and Zou, 2006; Bouvet, Castanié, Bizeul and Barrau, 2009; Lopes, Camanho, Gürdal, Maimí and González, 2009). These models need to be validated by comparing the experimental and numerical results. Basically, the validation of the developed approaches is classically limited to post-mortem damage footprints and global load responses (Topac, Gozluklu, Gurses and Coker, 2017) leading to a limited test-simulation dialogue. To better understand damage initiation and the interactions between transverse cracking and delamination that occur in LVI, various authors have used the approach initially proposed by Choi, Downs and Chang (1991). In this study, a simplified experimental configuration is used based on a line loading approach through the width of the specimen, reducing the problem to an almost 2D setting allowing monitoring of the damage initiation and growth on the side of the specimen. With the development in imaging capabilities, it is now possible to finely follow the initiation and propagation of damage for this specific test configuration (Topac et al., 2017). But to the authors knowledge, the application of high speed imaging to the classical LVI test configuration is not usually performed, or only with visible cameras for stereo-digital images correlation measurements (Namala, Mahajan and Bhatnagar, 2014; Flores, Mollenhauer, Runatunga, Beberniss, Rapping and Pankow, 2017; Cuyner, Scida, Roux, Toussaint, Ayad and Lagache, 2018), despite the fact that high speed infrared thermography is more and more used to quantify damage initiation and growth in composite materials (Chaibi, 2022; Battams and Dulieu-Barton, 2016; Johnston, Pereira, Ruggeri and Roberts, 2018; Portemont, Berthe, Deudon and Irisarri, 2018; Berthe and Ragonet, 2018; Pan, Wu and Xiong, 2019, 2020). Infrared thermography has been applied to LVI tests only to capture damage extension right after the test thanks to the thermal increase generated by damage growth during the impact (Meola and Carlomagno, 2009, 2010; Boccardi, Carlomagno, Simeoli, Russo and Meola, 2016; Meola, Boccardi and Carlomagno, 2018; Maierhofer, Krankenhagen and Röllig, 2019). Consequently, the objective of this study is to evaluate the capabilities of high speed infrared thermography to capture damage initiation and growth during impact tests for different energy levels. In Section 2, the experimental setup and the material of the study are going to be described. In Section 3, the results obtained with the high speed infrared thermography performed during the impact test at different energy levels will be analysed. In Section 4, an attempt to apply the classical methodologies for in-situ damage extension evaluation will be performed. In Section 5, classical post-mortem analysis mostly based on C-Scan and X-Ray tomographies will be performed and analyzed to establish some links between the thermal events and the damage mechanisms observed with other post-mortem instrumentation methods. Finally, in Section 6, the different projected damaged areas will be compared and some explanations regarding the differences will be proposed.

## 2. Materials and methods

### 2.1. Test specimens

The composite material considered in this study is the T700GC/M21 carbon/epoxy material provided by Hexcel with a weight area of 268 g/m<sup>2</sup>. The specificity of this material is that plies are interleaved with thermoplastic particles (cf. Figure 24). These particles delay the cracks propagation and, therefore enhance the material toughness. Specimens have been extracted from plates manufactured by hand lay-up and cured in an autoclave with the recommended cure cycle. A quasi-isotropic stacking sequence with 16 plies has been selected for this study: [(0/45/90/-45)<sub>2</sub>]<sub>s</sub> leading to an approximate specimen thickness of 4.3 mm. The in-plane dimensions are in agreement with the ASTM D7136 standard procedure: 150 mm × 100 mm. As shown in Figure 1, the specimens are simply supported on the impact window, with standard dimensions of 125 mm × 75 mm, in order to simplify the boundary conditions for future numerical simulations.

### 2.2. Experimental setup

The experimental setup used in this study is described in Figure 1. The impact testing machine is an Instron Dynatup 8250 equipped with an anti-rebound system, which has been specifically modified as shown on the left hand side in Figure 1 to allow for the direct installation of the high speed infrared camera to monitor the non-impacted surface. The hemispheric impactor 16 mm diameter is fixed to a guided trolley to reach a total mass of 13.01 kg. The load applied to the specimen is measured with a load cell with a maximum load of 22 kN. The displacement of the impactor is measured with a laser transducer and the speed of the impactor just before the contact is measured with a photoelectric sensor. The signals are directly recorded by the acquiring system of the impact machine. Two different infrared cameras have been implemented to capture images on the impacted face of the specimen with a CEDIP JADE III LWIR camera as well as on the opposite face with a TELOPS FAST M3k MWIR camera. More details regarding IR

cameras acquisition will be given in the following section. Finally, in order to ensure a time synchronisation between the load and displacement measurements and the images captured by the different cameras, a DEWESOFT acquisition system was used. The displacement of the impactor and the trigger (TTL signal generated from a top send by a push button) sent to the different cameras were recorded at 1 MHz by the acquisition system.

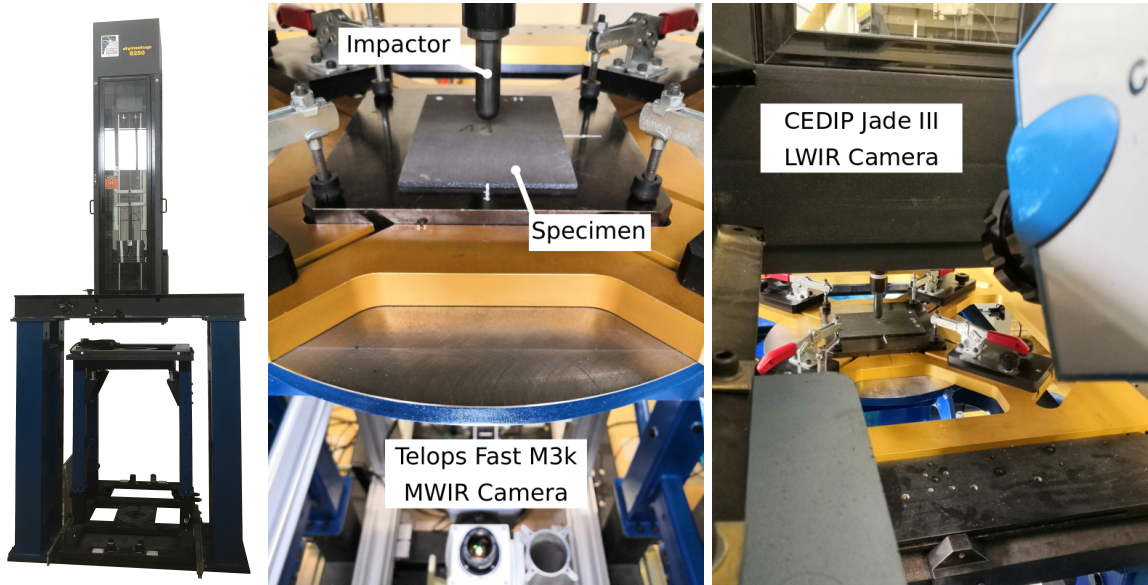


**Figure 1:** Experimental setup.

Four different energy levels have been tested: 6.5 J, 11 J, 20 J, 32 J. The different energy levels were obtained with a variation of the drop height based on the following expression:

$$h = \frac{E_i}{M_i g}$$

where  $E_i$  is corresponding to the targeted level of energy,  $M_i$  the total mass of the impactor and  $g$  the gravitational acceleration. The targeted level of energy  $E_i$  is also linked to the impactor velocity  $v_i$  just before the impact:  $E_i = \frac{1}{2} M_i v_i^2$ . For this study, four different impactor velocities have been used: 1.0 m.s<sup>-1</sup>, 1.3 m.s<sup>-1</sup>, 1.75 m.s<sup>-1</sup> and 2.32 m.s<sup>-1</sup>.

### 2.3. Infrared thermography

The two cameras used in this study are capable of high frame rate acquisitions even in full resolution. The CEDIP camera, which is the older one, can capture 320 × 254 pixels images at 300 Hz. The TELOPS camera can also capture 320 × 254 pixels images but at a maximum frame rate of 3000 Hz. By reducing the spatial resolution, the acquiring frequency of the two cameras can be increased up to 90 kHz for the TELOPS and 12.5 kHz for the CEDIP. Consequently, it has been chosen to use the Telops camera to monitor the opposite impact face on which more damage events are likely to occur. The different camera configurations (frame size, frequency and integration time 'IT') used in this study for the different considered energy levels are summarised in Table 1. These different parameters have been chosen in order to obtain a trade-off between the spatial and temporal resolution with the higher possible noise to signal ratio that can be achieved in this configuration. As it can be observed in Figure 1, the TELOPS infrared camera has been placed normal to the observed surface whereas the CEDIP camera has been placed with an angle of approximately 60° with respect to the normal of the observed surface due to the configuration of the impact machine. The emissivity of an object varies with the angle of observation, consequently for the CEDIP camera, the emissivity of the object is unknown with such an angle of observation. In the sequel, this camera will only be used for damage observation and the results are not going to be quantitatively analysed as temperature variations but only as Digital Level variations. For the TELOPS infrared camera, the composite plate is considered as a black body with a high

value of emissivity ( $\geq 0.95$ ). The temperature fields are obtained based on the integrated calibration performed by the manufacturer for the different lens and parameters of the camera. For the two different cameras, the analysis of the obtained fields will be mostly performed in a classical way, by comparing the field at a given time  $t$  with the initial field at a time  $t_0$  before the beginning of the impact test as proposed by Meola and Carlomagno (2009).

**Table 1**  
Infrared camera configurations for the different tests.

Infrared Camera	6.5 J	11 J	20 J	35 J
CEDIP	frequency : 3050 Hz	frequency : 3050 Hz	frequency : 3000 Hz IT : 70 $\mu$ s	frequency : 3050 Hz
TELOPS			frame size : 128 $\times$ 100 frequency : 12500 Hz IT : 9.96 $\mu$ s	

## 2.4. Post-mortem observations

In this study, *Post-mortem* observations have been performed in order to better analyse the different damage mechanisms occurring during impact test and to quantitatively quantify damage extension. Three different *Post-mortem* observation techniques have been used: SEM, C-scans and X-Ray tomography.

SEM observations were performed using a ZEISS Merlin with a field emission gun. A tension of 5 kV and an amperage of 5 nA were applied to the sample. Before observations, samples were cut using a diamond saw at 0° and 90° to visualize in these two planes the damaged topology. Once cut, the samples have been polished before observations using different Silicon Carbide (SiC) sanding papers until (0.25  $\mu$ m). The finish has been performed with a diamond-coated suspension.

The ultrasonic inspection was conducted at ONERA using an ultrasonic platform TPAC prelude. The sample was immersed in a water tank and clamped to an axis driven by 2 motors to translate the damaged sample regarding the fixed probe. A 5 MHz probe has been chosen with 128 cells. Each cell is spaced by 0.6 mm. C-scan in depth was carried-out to localize the damage mechanisms through the thickness. After the scan, the data has been processed and analyzed with the Extende Civa software. Gates have been created in order to capture the signal between the echoes at the entrance and exit of the plate.

X-ray  $\mu$ -tomographies have been performed at LMPS (Paris-Saclay Mechanics Laboratory) using a North Star Imaging (NSI) X50 250 kV computed tomography device. The system is equipped with a detector of 3072  $\times$  3888 pixels<sup>2</sup>, 14 bits with a cesium scintillator. X-rays were generated using a high-power focal spot (120 kV and 150  $\mu$ A). The data acquisition was carried out with an exposure time of 500 ms, 2000 projections with 20 frames per projection. All these parameters lead to a total acquisition time of 105 minutes. For each impact energy level, the size of the scanned volume is different and corresponds to the smallest volume containing all the damage mechanisms previously detected with C-Scan. Therefore, the 3D volumes were reconstructed with a voxel size of 13  $\mu$ m for the plate impacted at 11 J, 14  $\mu$ m for the plate impacted at 20 J and 16  $\mu$ m for the plate impacted at 35 J. The reconstruction has been performed using the commercial NSI software.

## 3. Results

In this section, the results obtained for the different energy levels are detailed. The analysis of the different test results are going to be performed with an increasing level of energy and consequently with an increasing complexity of observed damage phenomena.

### 3.1. Impact test at 6.5 J

The global response of the laminate plate for a 6.5 J impact test is plotted in Figure 2. On the left hand side, the load versus time curve exhibits a quite smooth loading and unloading phases with a duration of test of approximately 8 ms. On the right hand side, the loading and unloading phases are almost superposed leading to the conclusion that a very small amount of energy may have been dissipated during the test by damage growth within the composite plate.

## High speed infrared thermography for in-situ damage monitoring during impact test

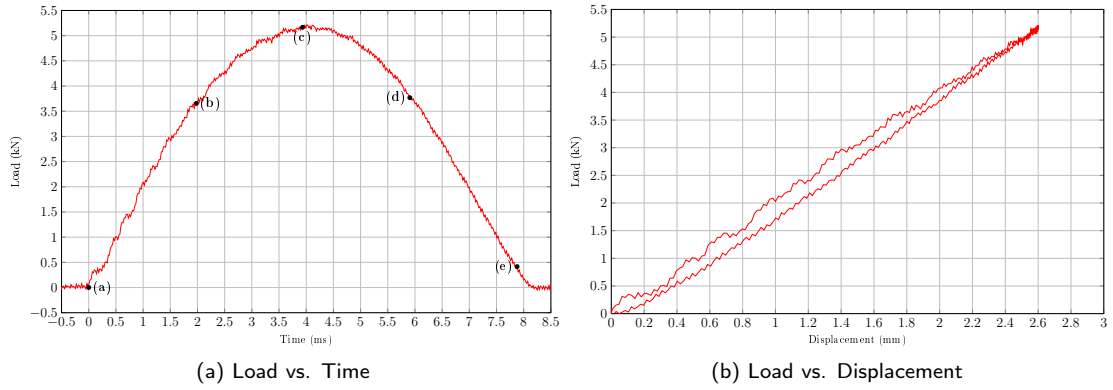


**Figure 2:** Global response of the composite plate for an impact test performed at 6.5 J.

For this test, the acquiring frequency of the CEDIP infrared camera has been fixed at 3050 Hz. Based on the test duration observed in Figure 2 and on the parameters described in Table 1, at least 24 images were captured by this camera during the test, whereas for the Telops camera, 100 images are taken during the test. An illustration of the IR images captured by the CEDIP camera during this test is plotted in Figure 3. It is possible to observe in these images horizontal lines with a fairly regular spacing. These lines are artifacts of the camera.

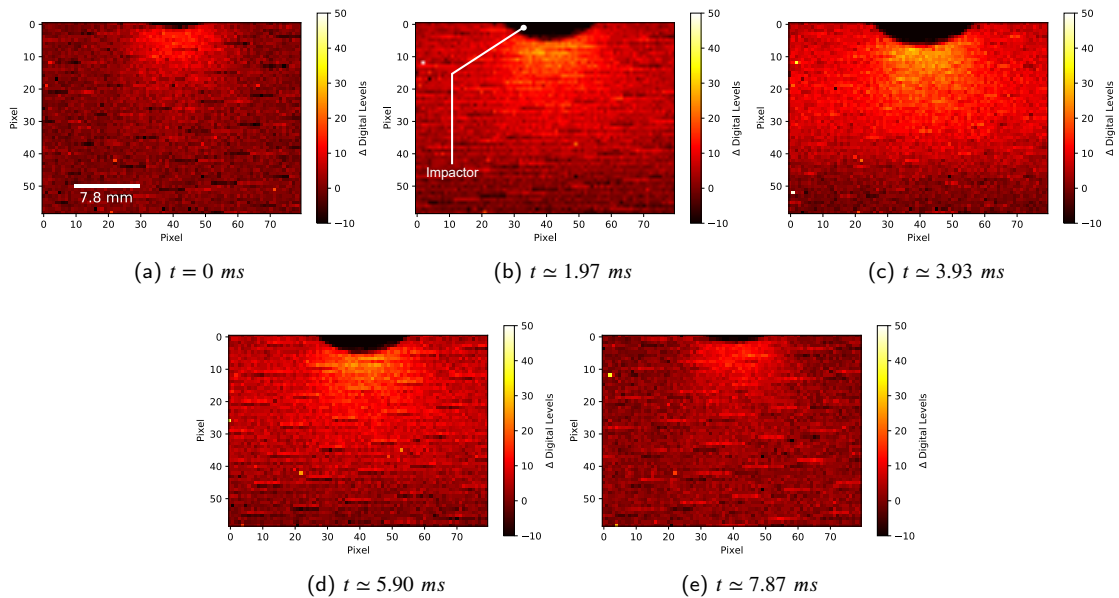


**Figure 3:** Infrared images captured by the CEDIP camera during the impact performed at 6.5 J.

First of all, the trigger system of the CEDIP camera is based on a quite old technology leading to around 100 ms temporal uncertainty. Consequently, the temporal synchronisation between the load and displacement signals and the CEDIP IR images is performed manually in a post test analysis phase. For that purpose, the mean variation of the digital level for a specific area of the specimen (all the pixels in the area between  $x \in [35, 45]$  pixels and  $y \in [12, 15]$  pixels in Figure 3) is computed for all the images and is directly compared to the load applied to the specimen. This specific area was arbitrarily chosen in the image in an area with loading-related signal and not in the path of the impactor during the test. The dimensions of this area were also chosen arbitrarily but with the desire to take a sufficient number of pixels in order to smooth out by averaging the temporal noise that each pixel can present individually. The two signals are

plotted in Figure 4 after treatment. It appears that a good correlation between the two signals can be obtained and, in the sequel, the time uncertainty linked to this procedure can be considered as the time between two images ( $1/3050 = 3.27 \cdot 10^{-4}$  s).

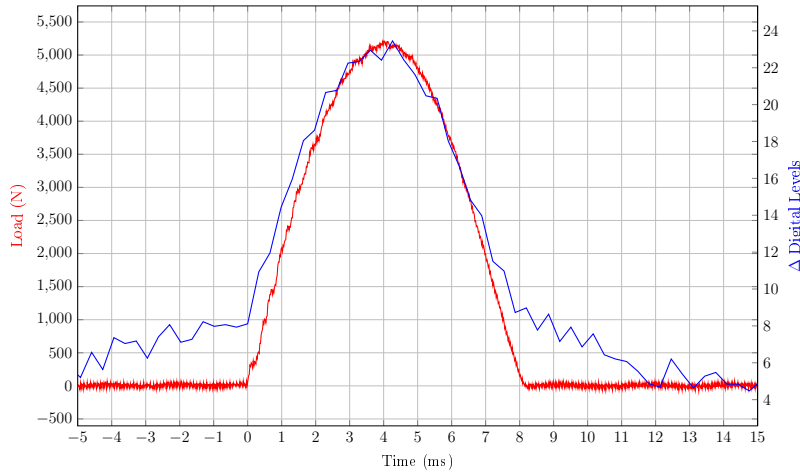


**Figure 4:** Time synchronisation between the load applied to the composite plate and the images taken by the CEDIP infrared camera.

It can be observed in Figure 4 that the mean variation of Digital levels given by the camera is already increasing before the load application on the composite plate and continues decreasing even after the end of the test. This may be due to the reflection of the impactor on the composite plate captured by the camera when the impactor is approaching the plate. This phenomenon can also be observed in Figure 3(a) at  $t = 0$  ms where the area close to the impactor exhibits higher DL variations than the rest of the plate. After that, when the plate starts to be loaded, an increase in the Digital Level is observed in Figure 4 and on the different pictures in Figure 3. This increase is linked to the thermoelasticity of the plate. The observed surface is mainly loaded in compression due to bending of the plate, which induces an increase of the temperature due to thermoelasticity. Finally, the last image in Figure 3 taken for a time close to the end of the test seems to exhibit almost no observable damage mechanisms on the observed area of the impacted surface.

The thermal field variations captured by the TELOPS infrared camera for some particular time instants are plotted in Figure 5. For  $t = 0$  ms, an homogeneous field is obtained with a mean value close to zero. After few milliseconds of loading, a decrease of the temperature in the middle of the plate is observed linked to thermoelasticity. Indeed, the observed surface is mainly loaded in tension due to bending which leads to a decrease of the temperature with thermoelasticity. With the image taken 2.8 ms after the beginning of the test, a crack on the surface of the composite plate is clearly observed. This crack is located in the middle of the plate, following the direction of the fibres in the  $0^\circ$ -outer ply. A small alignment default between the direction of the fibre in the surface plane and the horizontal axis of the IR camera can be observed on the image. For  $t = 4$  ms, the crack seems to be a bit longer than on the previous image. The crack is still surrounded by an area with an apparent decrease of temperature linked to the tensile loading of this surface ply. On the image taken at  $t = 9$  ms, the crack in the middle of the ply is still observable but as the load applied to the composite plate is now back to zero, the mean variation of temperature of the rest of the plate is back to zero. Finally, the acquisition has not been stopped right after the end of the loading, in order to be able to capture images after a hundred of milliseconds. These images can be compared to previous works performed on the use of infrared thermography during impact tests on composite materials (Meola and Carlomagno, 2009; Meola et al., 2018; Maierhofer et al., 2019). In this last image, an increase of the temperature can be observed in the middle of the sample, with an ellipsoidal shape which differs from the crack observed in previous images. In the literature, such a temperature increase after an impact test has been classically linked to damage extension area within the composite plate (Meola et al., 2018; Maierhofer et al., 2019). These authors have proposed various methodologies to quantify these areas and there is currently no standard procedure in the literature. Consequently, a specific study has to be done for this quantification and will be described in a dedicated section (see section 4).

Finally, the results can be summarised in Figure 6 in which the load applied to the specimen is directly linked to the different damage phenomena that can be observed by the different infrared cameras. In this case, as low impact energy

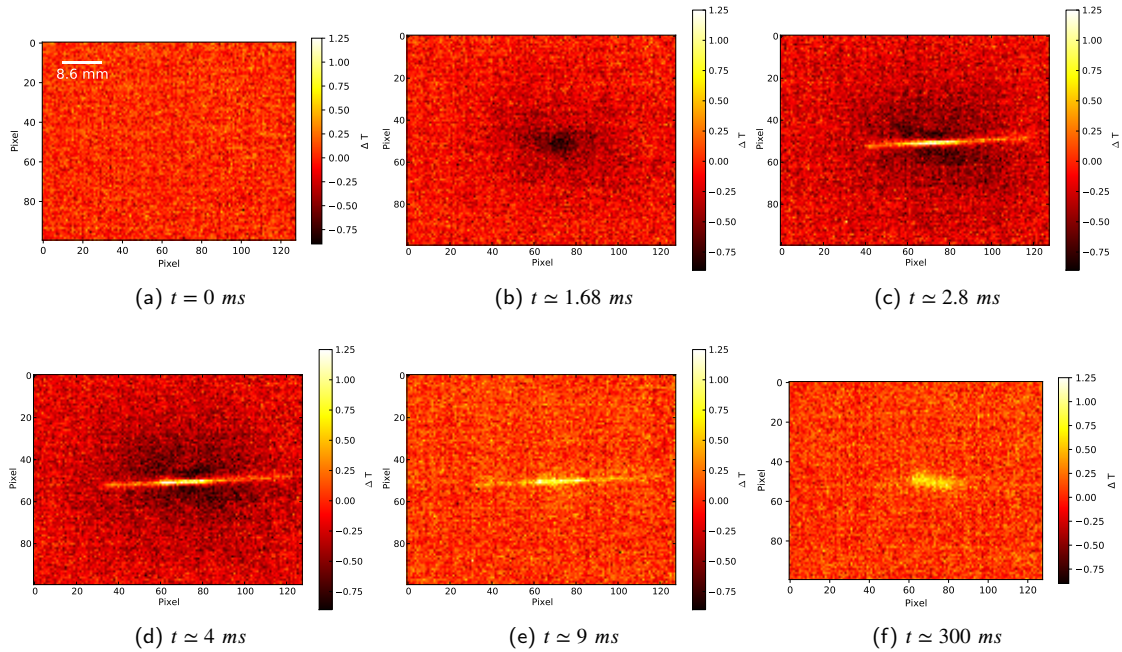


**Figure 5:** Temperature field variations captured by the TELOPS camera during the impact performed at 6.5 J.

level is considered, the main observable phenomenon is thermo-elasticity and a crack appearance on the opposite face for a load level around 3210 N. The crack opening is growing until the load peak. The infrared images captured on the impacted face do not appear to reveal any damage.

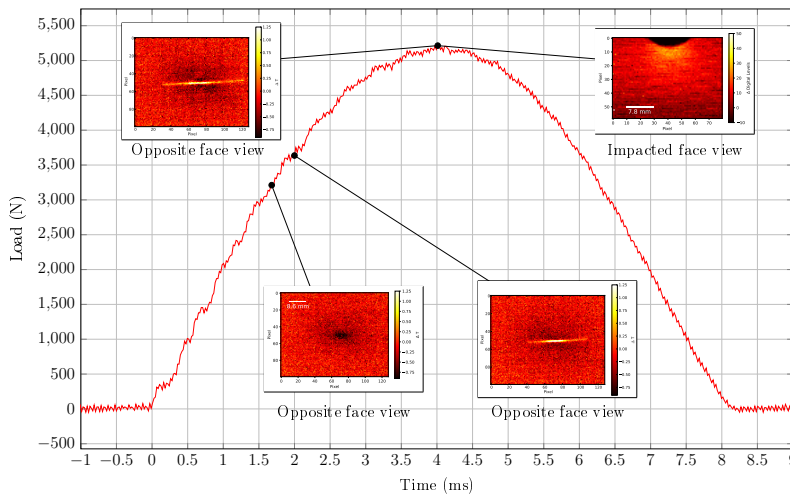


**Figure 6:** Cross analysis between the load applied to the composite plate and the images captured by the different infrared cameras for a 6.5 J impact test.

### 3.2. Impact test at 11 J

The global response of the laminate plate for a 11 J impact test is plotted in Figure 7. On the left hand side, the load versus time curve exhibits a quite smooth loading until approximately 6 kN where a small drop can be observed. The duration of the impact is approximately 8 ms. On the right hand side, the load versus displacement curve exhibits

more dissipated energy than for the test at 6.5 J. A sudden variation of the global slope of the loading phase is also observed in this figure at approximately 6 kN.

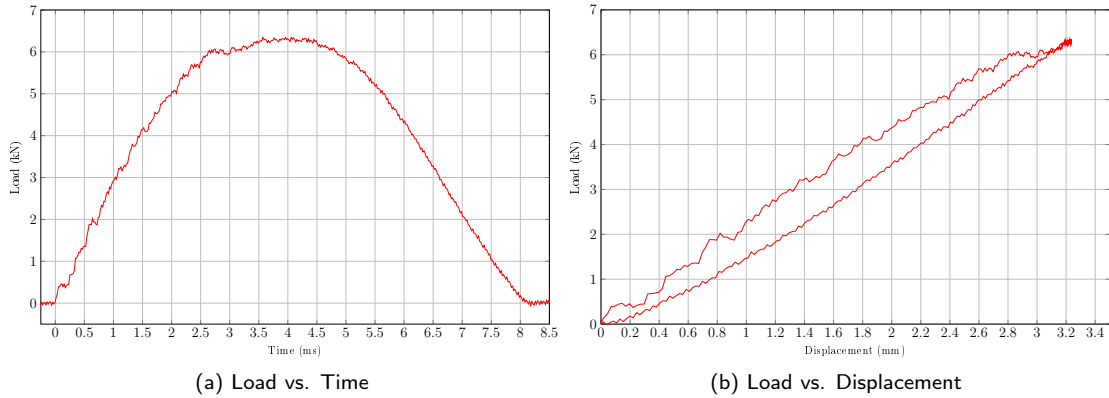


**Figure 7:** Global response of the composite plate for an impact test performed at 11 J.

First of all, a global analysis of the different images captured by the two infrared cameras can be performed with Figure 8. In a first stage, a global decrease of the temperature can be observed on the opposite face due to tensile load of the outer ply as for 6.5 J test. The first crack is observed for an applied load of 4131 N and the second one appears for an applied load of 4953 N. For an applied load higher than 6 kN, two new phenomena can be observed: some

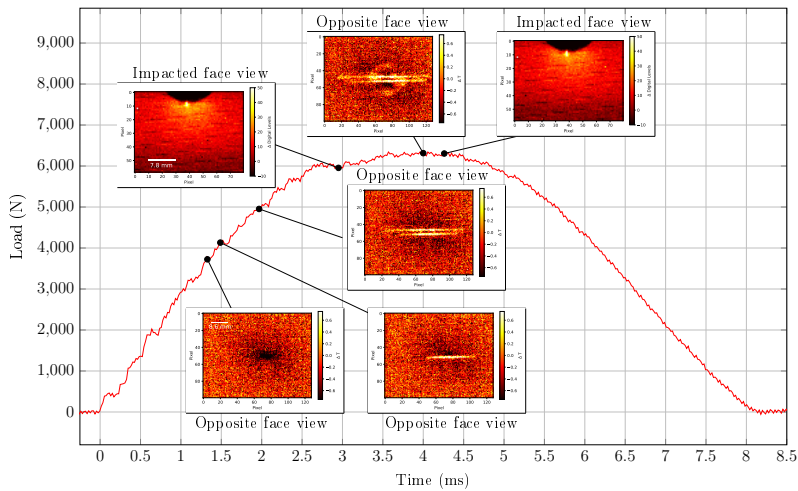


**Figure 8:** Cross analysis between the load applied to the composite plate and the images captured by the different infrared cameras for a 11 J impact test.

hot spots on the impacted face and a diffuse temperature increase with a circular shape on the opposite face. The hot spots observed on the impacted surface ply may be linked to compressive fibre failure in the surface ply in a direction perpendicular to the fibre orientation and will be confirmed with post-mortem observations in the sequel. This failure is captured with the infrared camera with the lower time resolution consequently, the uncertainty regarding the exact time appearance of this phenomenon is of approximately 0.33 ms. The failure appears on the image taken 2.9 ms after the beginning of the test and for an applied load of 5955 N. The second phenomenon with a diffuse circular shape below the impactor needs to be further studied to be understood. For that purpose, some infrared images captured on the opposite face between 2.5 ms and 4 ms after the beginning of the test are plotted in Figure 9. Apart from the two observable cracks, these images clearly exhibit the extend of the border of a circle starting for the middle of the impacted area. This circle is clearly observable as an increase of the apparent temperature on the non-impacted surface. For the last

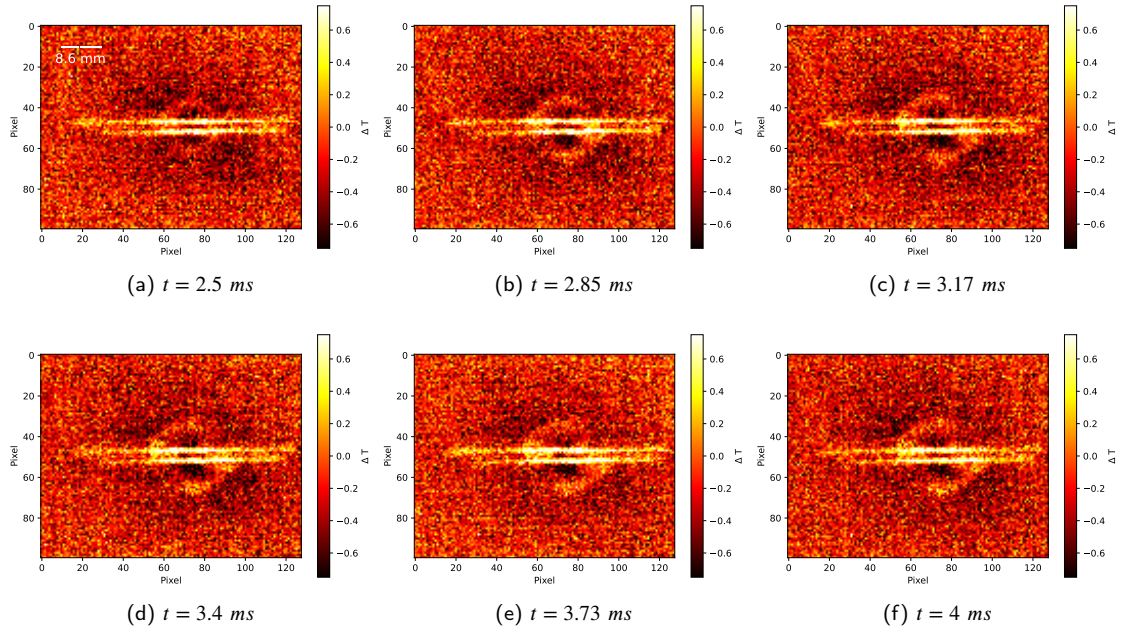


**Figure 9:** Temperature field variations captured by the TELOPS camera during the 11 J impact test between 2.5 ms and 4 ms.

two images, the shape appears to be more oval than circular with a long axis oriented at  $45^\circ$ . Moreover for these last two images, the propagation seems to be finished. This phenomenon can be compared to an image taken a long time after the beginning of the test as that plotted in Figure 10 taken for  $t = 300$  ms. The observed shape in Figure 9f is

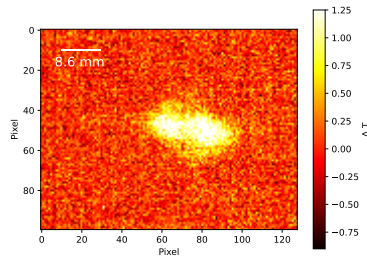


**Figure 10:** Temperature field variations captured by the TELOPS camera 300 ms after the beginning of the impact test.

clearly in good agreement with the shape observed in Figure 10 which is usually linked to the extension of impact damage as it was previously mentioned. Moreover, the shape observed in Figure 9f is similar to the shape classically observed for delamination during impact tests and could be correlated to the post-mortem damage analysis performed in Figure 25. Based on this observation, the extend of this phenomenon between 2.5 ms and 3.4 ms is probably linked to the propagation of delamination between the  $0^\circ$  surface ply and the adjacent  $45^\circ$  ply. Consequently, the small drop observed between 2.5 ms and 3 ms on the load curve can be explained by the two phenomena previously mentioned: a compressive failure observed on the impacted surface and the propagation of delamination between adjacent plies close to the opposite surface.

### 3.3. Impact test at 20 J

The global response of the laminate for the 2 tests performed at 20 J are plotted in Figure 11. The curves plotted on the left hand side exhibit a change of the loading slope for a load between 5.5 kN and 6 kN. The two curves are almost superimposed except for the appearance of the slope change between 5.5 kN and 6 kN. Compared to lower

impact energy tests, larger oscillations can be observed, particularly between 4 and 4.5 ms. On the right hand side of Figure 11, the load versus displacement curve are also superimposed except between 5.5 kN and 6 kN.

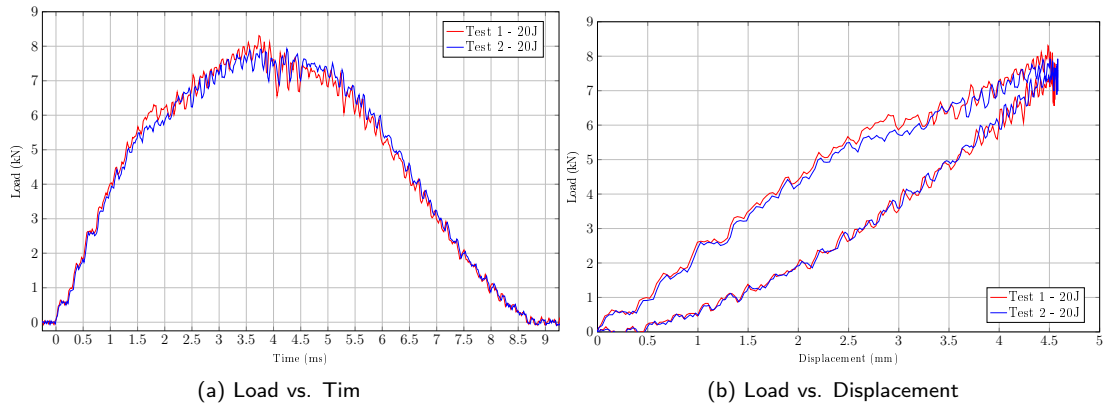


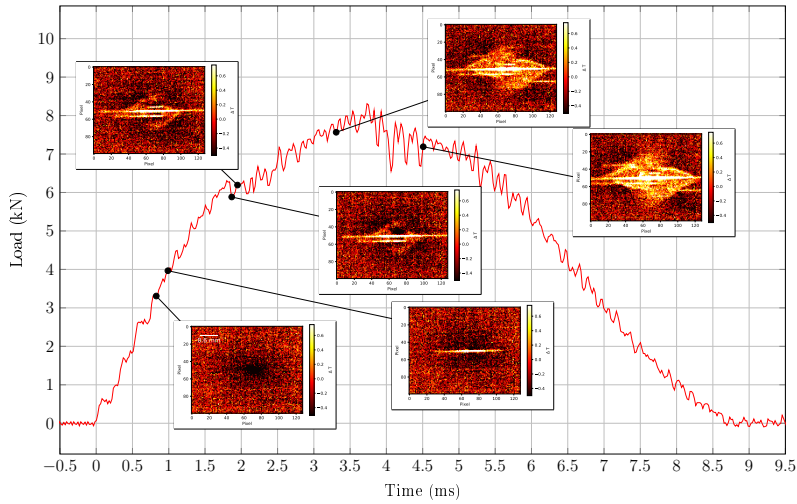
**Figure 11:** Global response of the composite plate for the 2 impact tests performed at 20 J.

In the first instance, only one of the two tests is going to be deeply analysed regarding the IR images. In a second instance, a specific focus on the variations between the two tests will be performed in a dedicated subsection. For the test previously referred as "Test 1 - 20 J", a global analysis of the different images captured by the two infrared cameras can be performed using Figure 12. As it was already mentioned for the test at 11 J, the slope change observed for loads higher than 6 kN can be linked to the growth of delamination which can be observed on the opposite face but also to a compressive fibre failure observed on the impacted face. On the left hand, it can be observed that the extend of delamination and the number of cracks is higher than for tests at lower energies. Moreover, the shape of the delamination appears to be in agreement with those classically observed in such impact tests (Bouvet et al., 2009; Troussset, 2013). A higher extend of the compressive failure is also observed on the right hand side of Figure 12. All these observations are in good agreement with the higher dissipated energy level which can be observed in Figure 11.

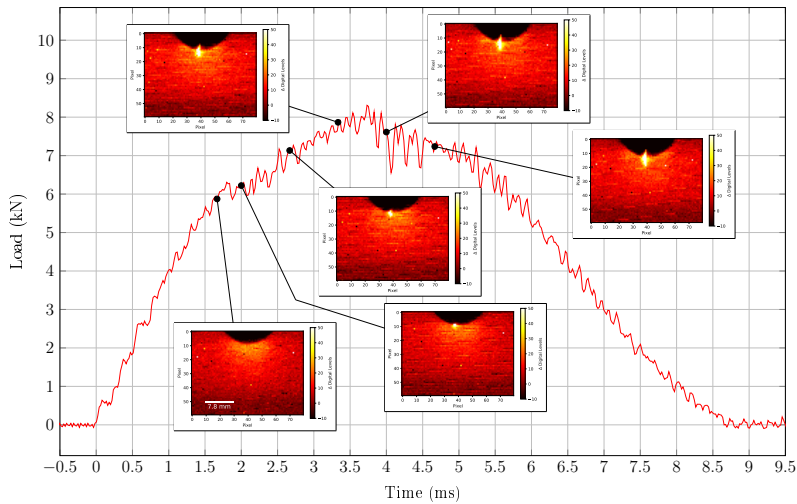
A specific focus is done in Figure 13 in order to analyse the highest level of oscillations observed between 3.7 ms and 4.5 ms in Figure 11. For that purpose, the analysis of the thermal fields has to be modified in order to exacerbate the phenomenon that happen between two captured images. Consequently, the temperature difference plotted in Figure 13 is obtained by making a difference between the image captured at the time  $t$  and the image previously captured at the time  $t - (1/12500)$ . These images clearly show that an important amount of energy is released as heat between  $t = 3.71 \text{ ms}$  and  $t = 3.79 \text{ ms}$ . An important increase of the temperature (between  $6^\circ\text{C}$  and  $20^\circ\text{C}$ ) can be observed within the central crack of the specimen. Such an increase of temperature has not been observed previously for the damage phenomenon observed on the opposite face. Therefore, it seems likely that this phenomenon is related to a sudden failure event with a significant amount of energy released, such as tensile fibre failure below the surface ply. This assumption has been confirmed with the post-mortem analysis that will be described in details in the sequel. Finally, for the last two images in Figure 13, some hot points can be observed which are linked to some debris generated by the event observed at  $t = 3.79 \text{ ms}$  and which are flying within the images taken after this event.

### 3.4. Variability between two tests performed at the same impact energy

As it was previously mentioned, the two loading curves plotted in Figure 11 are almost superimposed except between 5.5 kN and 6 kN, for times between 1.5 ms and 2.2 ms. Based on this observation, the variation of the thermal fields for the two tests for this specific interval of time are plotted in Figures 14 and 15. First of all, a small difference in the orientation of the tested specimens can be noticed based on the inclination of the main central crack particularly for the second test. This difference in the alignment of the two specimens can explain the very small difference which can be observed between the two curves before 1.5 ms which is linked to the apparent stiffness of the coupon. Apart from this difference, the two figures exhibit a damage scenario which is quite similar. Moreover, the different crack appearances are almost synchronised. For the second test plotted in Figure 15, the delamination growth seems to be quicker than for the first one. Indeed, for the first five images in Figure 15, the delamination area seems to be larger than for the first five images in Figure 14. This is the only difference that can be observed in these images regarding



(a) Images captured by the infrared cameras on the opposite face



(b) Images captured by the infrared cameras on the impacted face

**Figure 12:** Cross analysis between the load applied to the composite plate and the images captured by the different infrared cameras for an impact test performed at 20 J.

damage growth. This difference may explain why the load curve for the second test is lower between 1.5 ms and 2.2 ms than that for the first test, as the damage appears to grow more rapidly during this test. The comparison for the two tests of the images captured for the impacted surface during such a small time interval is not relevant because of the lower time resolution.

A comparison can also be performed for the instant of appearance of the brutal failure event previously mentioned. For the test referred as "Test 1 - 20 J", the event appears between  $t = 3.71 \text{ ms}$  and  $t = 3.79 \text{ ms}$ . This interval of time can be linked to an interval of load which is between 7818 N and 7983 N. The same analysis can be done for the second test. It leads to the appearance of the brutal failure event between  $t = 3.57 \text{ ms}$  and  $t = 3.65 \text{ ms}$ . This interval of time can be linked to an interval of load which is between 7349 N and 7836 N. A small difference between the two tests is observed but does not appear significant.

### 3.5. Impact test at 35 J

The global response of the laminate plate for a 35 J impact test is plotted in Figure 16. As it was previously observed, the loading slope exhibits a first decrease between 5.5 kN and 6 kN. After 2.5 ms and for a load of approximately 8

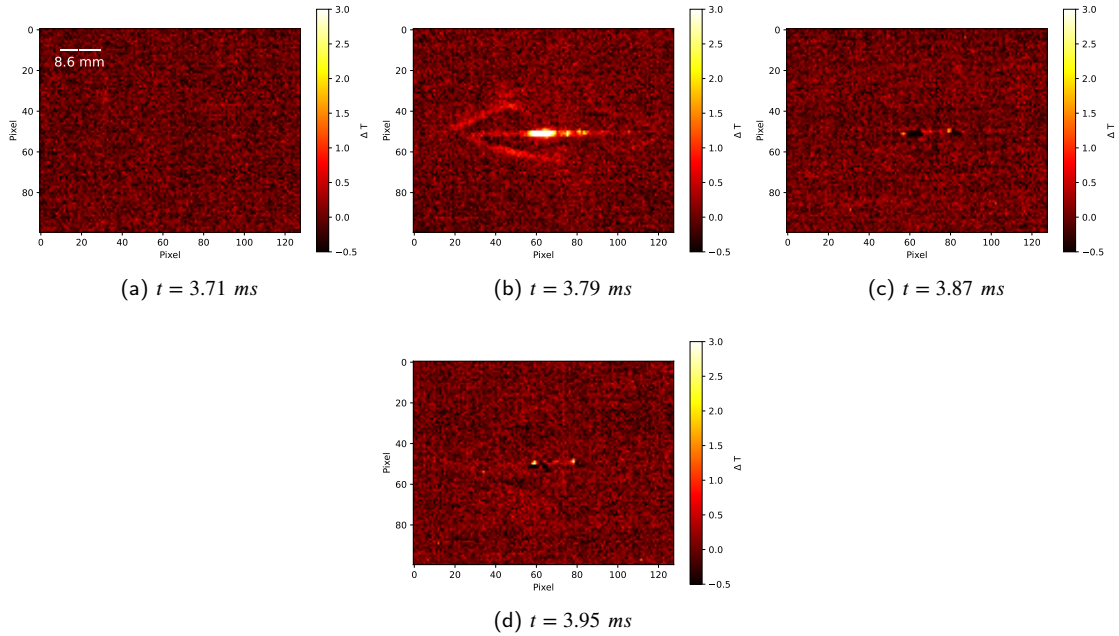


**Figure 13:** Temperature field variations captured by the TELOPS camera during the 20 J impact test between 3.71 ms and 3.95 ms.

kN, the load exhibits important oscillations. Such oscillations have also been observed in Figure 11 for the 20 J impact tests for an equivalent load level. As it can be observed on the right hand side of Figure 16, even if the displacement is still growing after the first important oscillation, the load does not seem growing anymore.

First of all, a global analysis of the different images captured by the two infrared cameras can be performed with Figure 17. As it was already mentioned for the tests at 11 J and 20 J, the change in slope observed for loads above 6 kN may be related to the growth of delamination that can be observed on the opposite side but also to the failure of the fibre in compression observed on the impacted side. Indeed, in the figure on the right, even if this compression failure is not very extensive for 6 kN, it is still visible. For the delamination, in the figure on the left, an important extension of the delamination can be observed between 6 and 7.5 kN. With this figure, it can also be observed that the damage extension during the 35 J test is larger than the observation window used in this experimental investigation for the Telops IR camera. Finally, based on Figure 17, the interpretation of the large oscillations observed after 2.5 ms is not obvious. As it was previously done for 20 J test analysis, a specific post-treatment can be applied to better understand the important oscillations that can be observed after 2.5 ms. For that purpose, the images plotted in Figure 18 have been analysed by making the difference between the image captured at the time  $t$  and the image previously captured at the time  $t - 1/12500$ .

These images clearly exhibit a brutal failure event below the surface of the laminate as it was also observed for the 20 J impact test. Post-mortem analysis will confirm, in the sequel, fibre failures below the surface of the specimen which may be linked to this high energy event. As these events occur below the IR observable surface, the diffusion phenomena require a sufficiently long time to allow the surface observation of these events. In a previous work (Berthe and Ragonet, 2018), diffusion time through one  $0^\circ$  ply of the composite material studied in this work has been qualitatively evaluated. After a time between 39 ms and 52 ms, the thermal increase due to the propagation of a transverse crack that has propagated below the  $0^\circ$  degree ply is clearly observable on the surface of this ply. Based on this result, a specific analysis of the images taken after the end of the test can be proposed in order to observe the temperature variation due to diffusion through the thickness. The images plotted in Figure 19 have been obtained by making the difference between the IR images taken at  $t_1 = t_{end} + 45 \text{ ms}$  (diffusion through 1 ply) or  $t_2 = t_{end} + 90 \text{ ms}$  (diffusion through 2 plies) and the IR image taken at  $t_{end}$ . The different images have been plotted based on the same interval for the colorbar. Firstly, it clearly appears that the area, in which the temperature increases are observed, is increasing with the energy applied to the specimen. For the three different energy levels, a quite homogeneous temperature increase

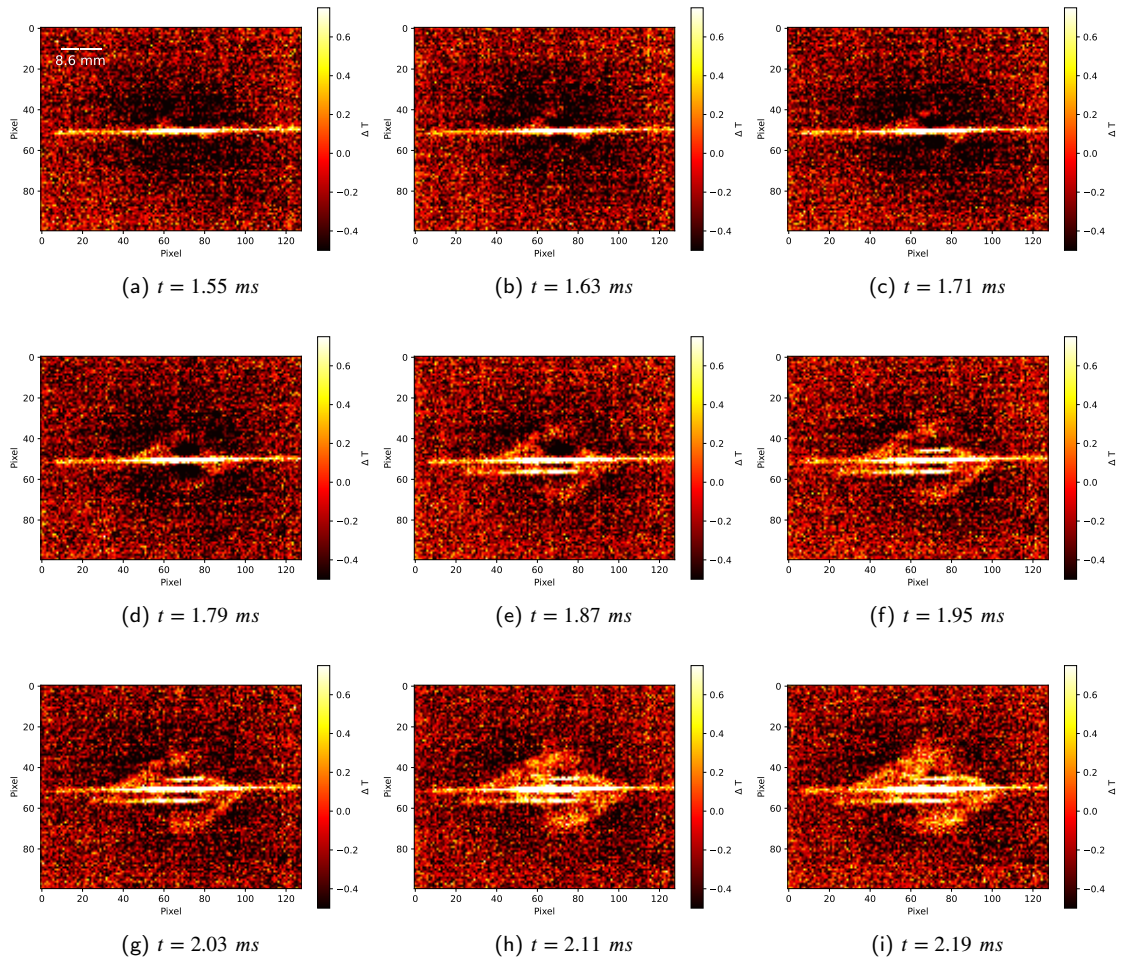


**Figure 14:** Temperature field variations captured by the TELOPS camera during a 20 J impact test (Test 1) between 1.5 ms and 2.2 ms.

can be observed, with a typical delamination shape for such a quasi-isotropic laminate under impact. The size of this area is increasing with the energy and can be compared to post-mortem analysis performed in the sequel and particularly to Figure 25. The shape is clearly linked to the delamination between the last two plies on the side opposite of the impact. Secondly, more significant but this time more localized temperature increases can be observed with increasing impact energy levels (20 J and 35 J). In particular, a rather chaotic line seems to be drawn in the center of the specimen with a rather small angle to the vertical. A second line with an angle of  $45^\circ$  is also observed for the 20 J and 35 J tests. These two high temperature lines are not observed for the 11 J impact test. These dissipative phenomena appear for higher energy levels and therefore for higher applied forces. The more important oscillations on the stress signal observed on the 20 J and 35 J tests could therefore come from these phenomena. Considering their topology with respect to the studied stacking sequence, these dissipative phenomena seem to be linked to fibre breaks that could have been observed with the help of a post-mortem analysis. This specific analysis methodology is quite similar to other works in the literature whose objective is the analysis of damage extension during impact tests using infrared thermography (Meola and Carlomagno, 2010; Boccardi et al., 2016; Meola et al., 2018; Maierhofer et al., 2019). These methodologies will therefore be applied to our tests in the following.

## High speed infrared thermography for in-situ damage monitoring during impact test

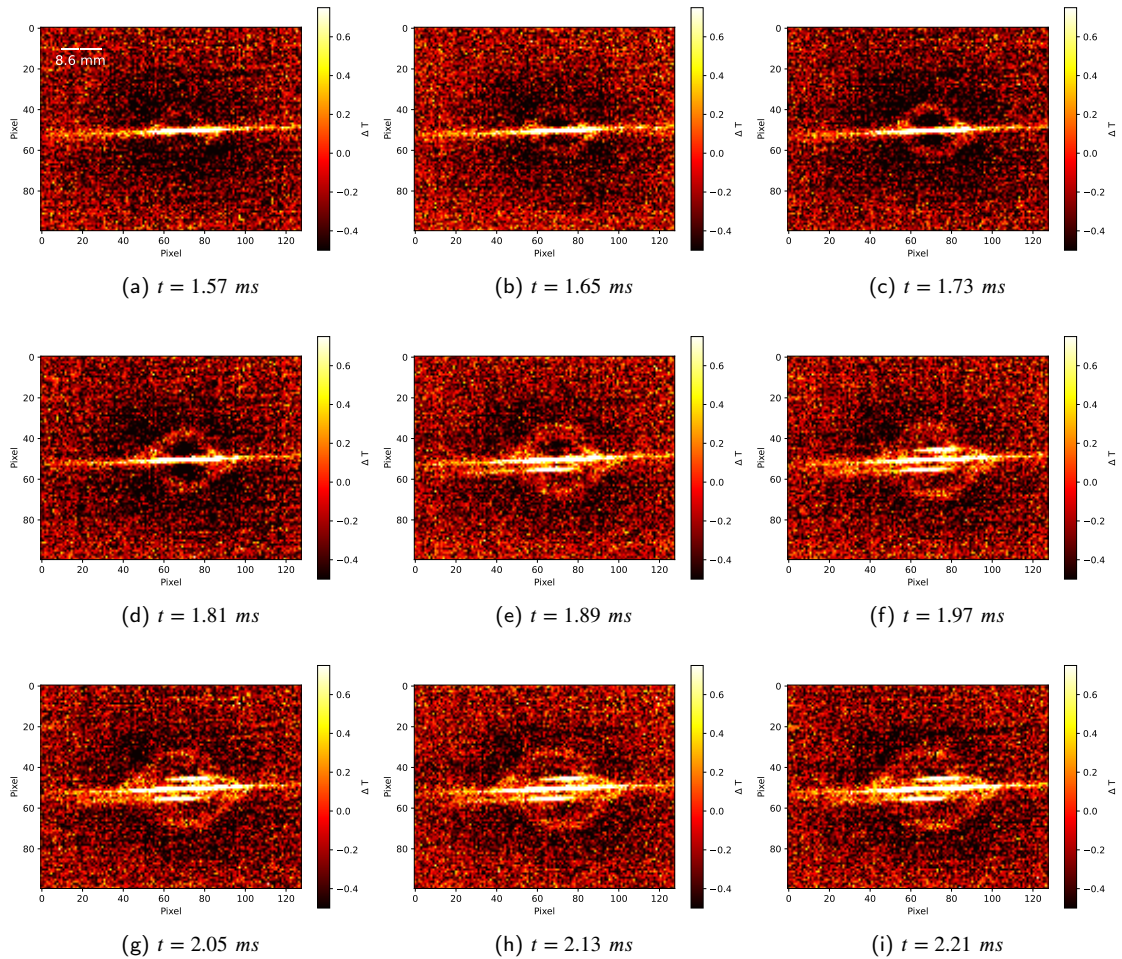


**Figure 15:** Temperature field variations captured by the TELOPS camera during a 20 J impact test (Test 2) between 1.5 ms and 2.2 ms.

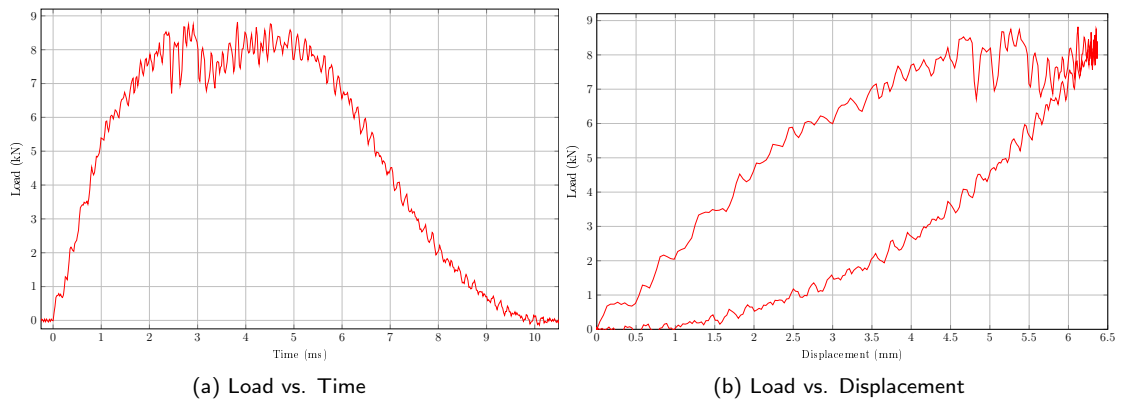
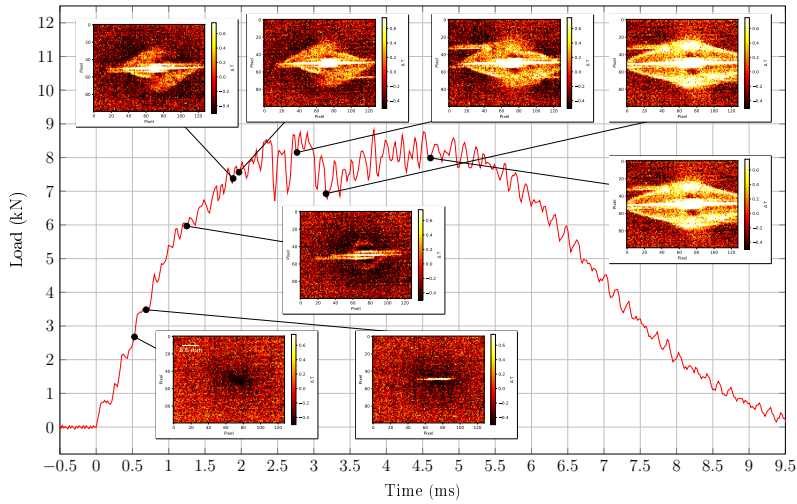
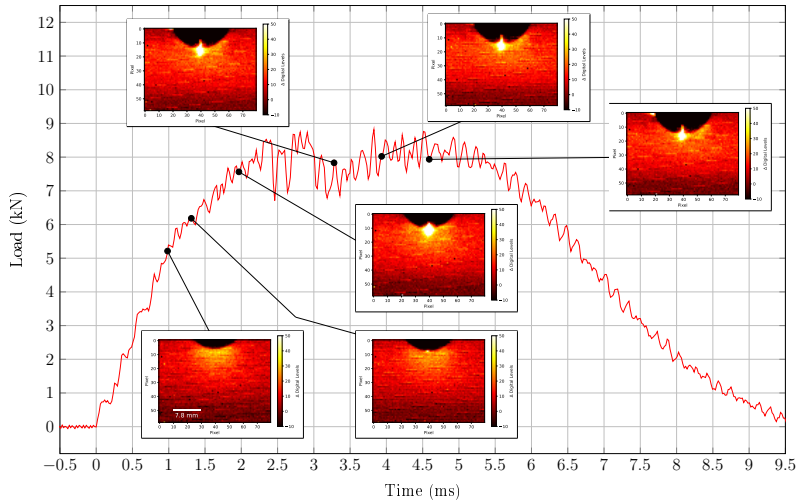


**Figure 16:** Global response of the composite plate for an impact test performed at 35J.



(a) Images captured by the infrared cameras on the opposite face



(b) Images captured by the infrared cameras on the impacted face

**Figure 17:** Cross analysis between the load applied to the composite plate and the images captured by the different infrared cameras for an impact test performed at 35J.

#### 4. Damage extension evaluation

Various methodologies are available in the literature in order to evaluate the damage extension during impact tests based on infrared thermography measurements (Meola and Carlomagno, 2010; Boccardi et al., 2016; Meola et al., 2018; Maierhofer et al., 2019). These investigations have been performed with lower acquiring frequency but therefore for longer periods of time. Typically in Meola et al. (2018), the damage extension for CFRP plates is evaluated for images captured more than 0.5 s after the beginning of the test. Due to the higher acquiring frequency used in this study, in most of the tests, the acquisition of IR images on the opposite face was stopped between 0.4 s and 0.5 s after the beginning of the test. The variation is due to the fact that the acquisition of the different cameras is manually launched during the tests by an operator with a push button which generates a TTL signal for the cameras. Such a long period of time is used in order to ensure that the dissipated energy has reached a plateau. Moreover, this quite long period of time allows the heat generated by damage within the thickness of the plate to diffuse up to the monitored surfaces of the plate. As in this study the acquiring time is shorter, the choice has been made to not extrapolate the results to a longer period of time and to evaluate the damage extension on the last captured image. Consequently, the reader has to keep

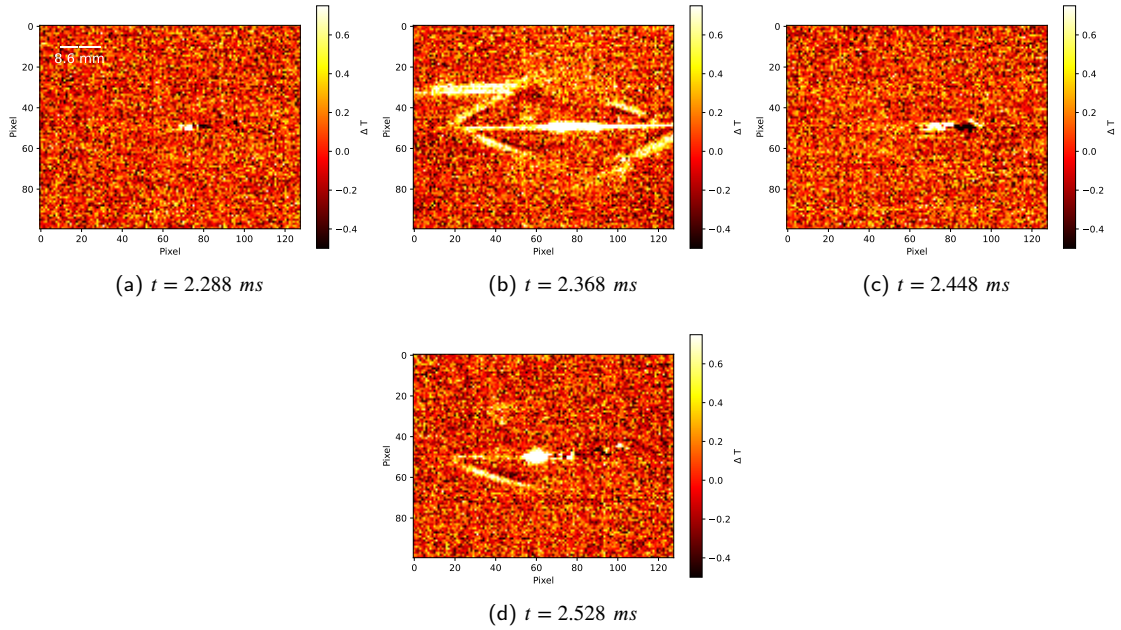


**Figure 18:** Temperature field variations between two successive images captured by the TELOPS camera during the 35 J impact test between 2.288 ms and 2.528 ms.

in mind that the results regarding the damage extension based on IR measurement in this study may be underestimated with respect to the already available studies (Meola and Carlomagno, 2010; Boccardi et al., 2016; Meola et al., 2018; Maierhofer et al., 2019). Secondly, these studies have been performed with higher integration times, typically 1.12 ms for Maierhofer et al. (2019), which allow increasing the signal to noise ratio. Due to the high acquisition frequency used in this study, the integration time used to acquire the IR images is  $9.96 \mu\text{s}$  leading to higher noise level in the captured images. To illustrate the consequences, the methodology proposed by Maierhofer et al. (2019) is applied for the impact test performed at 6.5 J. The different steps of the methodology are not going to be recalled in the sequel, the reader may refer to the section 3.3.2 in Maierhofer et al. (2019) for more details. The results obtained for an image captured 425.12 ms after the impact are plotted in Figure 20 and should be compared to Figure 2 in Maierhofer et al. (2019). First of all, it clearly appears in Figure 20a, that the noise in the thermogram is clearly higher in this study. Consequently, the obtained histogram has a different shape leading to a  $j_2$  value (which the right border at the full width at half maximum of the histogram peak) around 60 instead of 20 for Maierhofer et al. (2019). Finally, the heated area matrix exhibits a non continuous area in the center of the image and includes more than 10 pixels randomly localised in the image. A specific focus, can be made on a pixel in the center of the image, referred as Pixel b in Figure 21a, which has not been selected by the Maierhofer's methodology as a heated one, for example the pixel  $x = 69$  and  $y = 49$ . The evolution of the apparent temperature of this pixel is plotted in Figure 21 on the left hand side and can be compared on the right hand side to the pixel  $x = 57$  and  $y = 37$  (referred as Pixel a in Figure 21a) which is not in the apparent heated area. The two thermograms present some similarities before the impact test with for example a mean apparent variation of temperature around 0 K with a noise variation approximately between  $[-0.25\text{K}, 0.25\text{K}]$ . The impact test is clearly visible with the negative pic with a minimal value of apparent temperature of  $-0.75\text{K}$ . However, after this impact test, the two thermograms differ. For the pixel  $x = 57$  and  $y = 37$ , the mean apparent variation of temperature comes back to zero whereas for the pixel  $x = 69$  and  $y = 49$ , the mean apparent variation of temperature slowly increases and finally stabilises between 0.4 K and 0.5 K. Despite of the important noise, these two pixels exhibit a clear difference in the post impact behaviour and the pixel  $x = 69$  and  $y = 49$  should be included in the heated area matrix which is not the case with the methodology developed by Maierhofer et al. (2019). Consequently, a specific treatment of the data has to be proposed for this study to evaluate the heated area extension which can be observed during these tests.

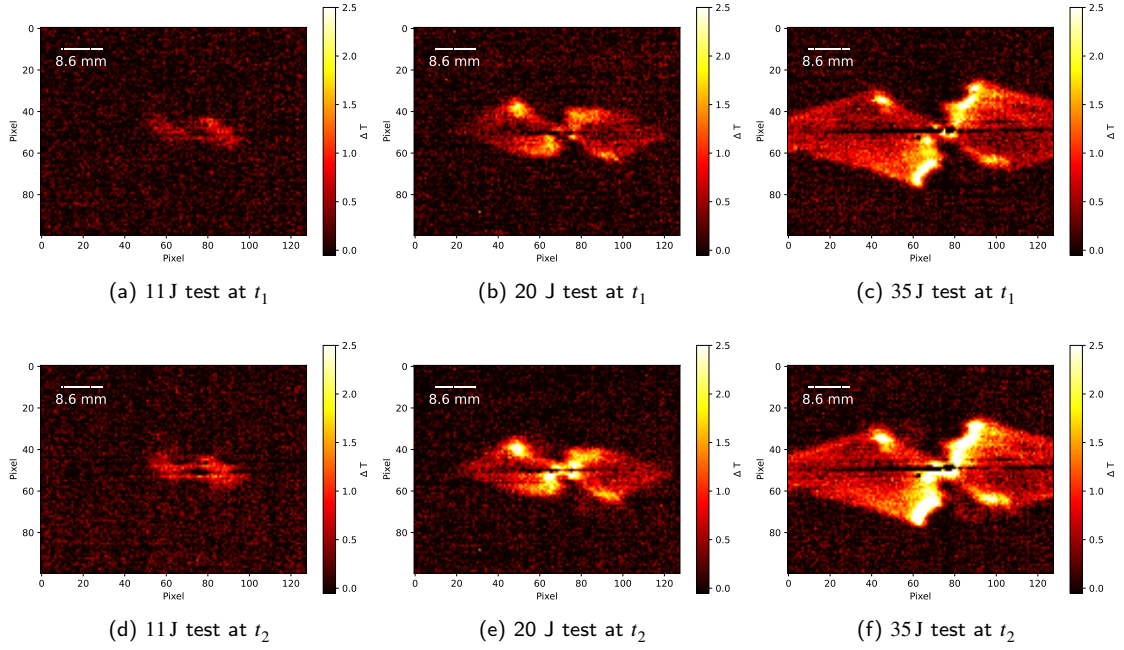


**Figure 19:** Temperature field variations between the end of the test and two particular times  $t_1$  and  $t_2$  for different impact energy levels.

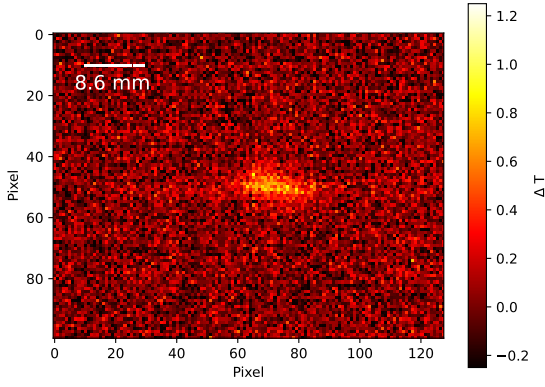
#### 4.1. Determination of the heated area

In order to evaluate the heated area after the impact, the high temporal discretisation used for the study of damage appearance during the impact test is no longer mandatory. Consequently, a data reduction can be performed based on the average value of the pixel over a given number of frames. As shown in Figure 22, a drastic reduction of the apparent noise for the selected pixel ( $x = 69$  and  $y = 49$ ) is observed by using an average value over 20 images. In that case, the apparent noise observed in Figure 22 appears to be in better agreement with the order of magnitude classically observed in the literature. Based on that observation, *the reference based method* proposed in Boccardi et al. (2016) will be used in the sequel to evaluate the heated area with the post-treated IR data obtained after the data reduction process. This choice is based on the fact that this methodology appears to the author as the simplest one and as it was mentioned by Maierhofer et al. (2019) the results obtained with the different methodologies are very similar. The analysis methodology proposed by Boccardi et al. (2016) will be briefly recalled. First of all, a reference image before the beginning of the test is generated based on an average value of each pixel over a given number of frames (100 in the work of Boccardi et al. (2016)). Due to the data reduction already performed on the results, only 50 images can be used in this study to build the reference image before the test:

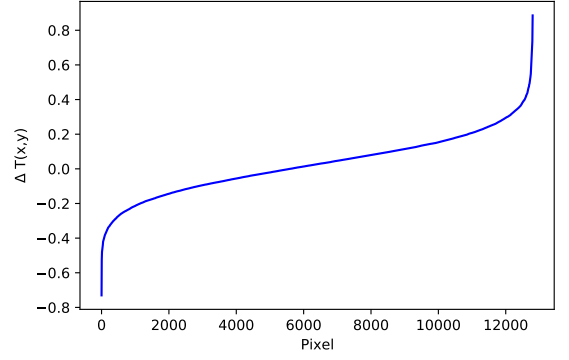
$$\Delta T_R(i, j) = \frac{1}{50} \sum_{t=1}^{50} \Delta T(i, j, t) \quad (1)$$

This average reference image allows reducing the dependency of the reference to the observed noise. The standard deviation  $\sigma_{i,j}$  of each pixel over the same 50 images is also computed. It will be used to defined the threshold value  $\Delta T_{Ti,j}$  for the determination of damage extension by assuming  $\Delta T_{Ti,j} = 3\sigma_{i,j}$ . The determination of the heated area is also based on an average value of  $\Delta T$  over a given number of images. Typically, 50 images are used in Boccardi et al. (2016). This average value will be called *warm image* and noted  $\Delta T_W(i, j, t_i)$ :

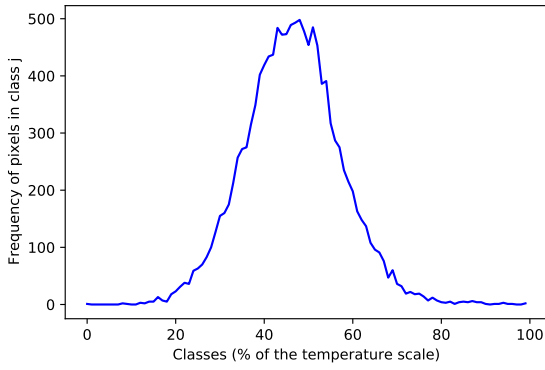
$$\Delta T_W(i, j, t_i) = \frac{1}{50} \sum_{t=t_i}^{t_i+49} \Delta T(i, j, t) \quad (2)$$



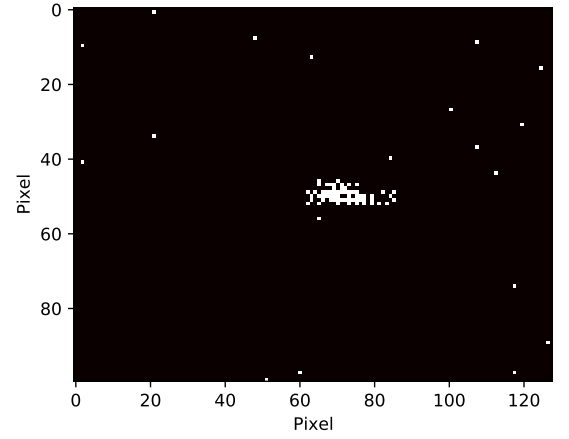
(a) Selected thermogram for the application of the analysis methodology proposed by Maierhofer et al. (2019)



(b) Resorted temperature values of the plotted thermogram.



(c) Histogram of the frequency of pixels belonging to each class. Classes 1 to 100 comprise the temperature from  $T_{min}=-0.73K$  and  $T_{max}=0.89K$ .



(d) Heated area matrix obtained with this approach.

**Figure 20:** Results obtained in this study with the analysis methodology proposed by Maierhofer et al. (2019) which can be directly compared to the results plotted in Figure 2 in the original paper.

Finally, the heated area matrix  $Md(i, j, t_i)$  can be created based on the following mathematical criteria:

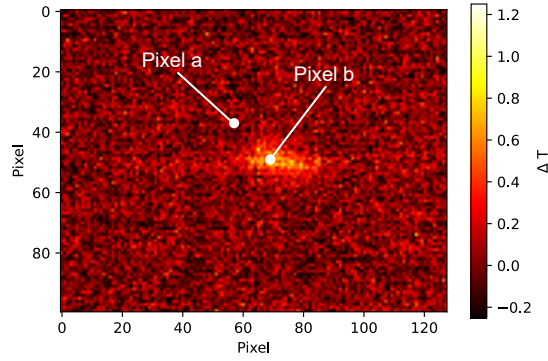
$$Md(i, j, t_i) = \begin{cases} 1 & \text{if } \Delta T_W(i, j, t_i) \geq \Delta T_R(i, j) + 3\sigma_{i,j} \\ 0 & \text{if } \Delta T_W(i, j, t_i) < \Delta T_R(i, j) + 3\sigma_{i,j} \end{cases} \quad (3)$$

As it was previously mentioned, in this study the sequence duration is shorter than those classically used by the different authors previously mentioned. In order to be as close as possible to the recommendations proposed by Meola et al. (2018), the last computational time (referred as *Evaluation instant*) of the heated area matrix will be used in the sequel to obtain the results summarised in Figure 23 and Table 2. First of all, as it was previously observed for the 35 J

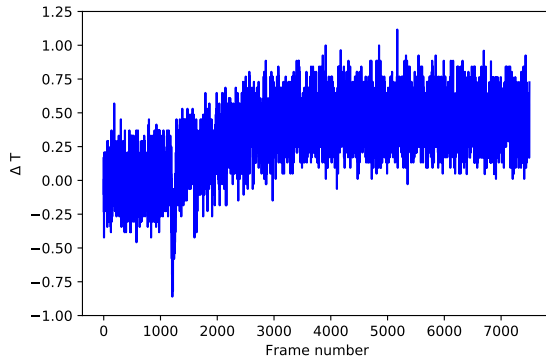
**Table 2**

Results of the damage extension evaluation method for the different impact tests performed in this study.

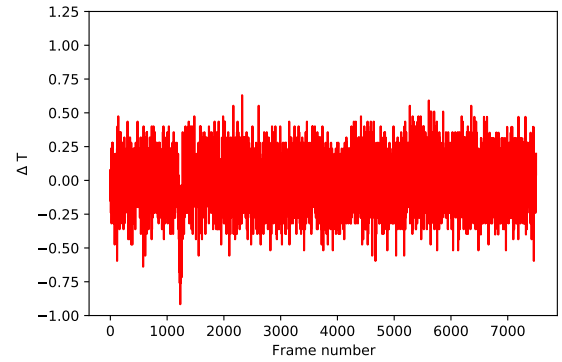
	6.5 J	11 J	20 J - Test 1	20 J - Test 2
Heated area	67.86 mm <sup>2</sup>	271.95 mm <sup>2</sup>	698.92 mm <sup>2</sup>	656.95 mm <sup>2</sup>
Evaluation instant	0.4243 s	0.3885 s	0.3820 s	0.4005 s



(a) Positions of two selected pixels in the studied image



(b) Thermogram of the pixel  $x = 69$  and  $y = 49$  (Pixel b)



(c) Thermogram of the pixel  $x = 57$  and  $y = 37$  (Pixel a)

**Figure 21:** Comparison of the thermograms for two pixels located in two different positions.

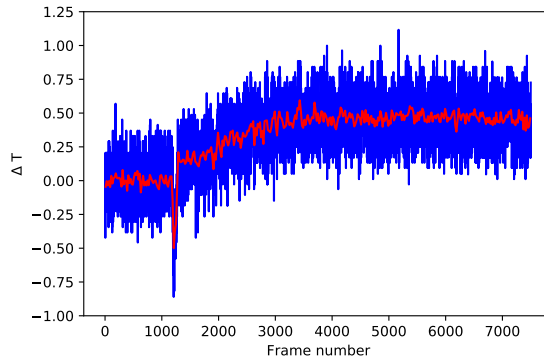


**Figure 22:** Comparison between the raw thermogram and the one obtained with an average value of the pixels over 20 images.

test, the damage extension appears to be larger than the area observed by the IR sensor. Consequently, the area is not evaluated for this test. As it was previously observed by the different authors mentioned in this work, the heated area increases with the impact energy. It can be noticed for the two tests performed at 20J that the results are quite similar with a variation of less than 10% of the heated area between the two tests. The shape of the damaged area is globally the same between the different tests, only the size of this area is changing. Finally, it appears for the two 20J impact tests that the size of the images starts to become too small to be able to capture all the observable heated area.

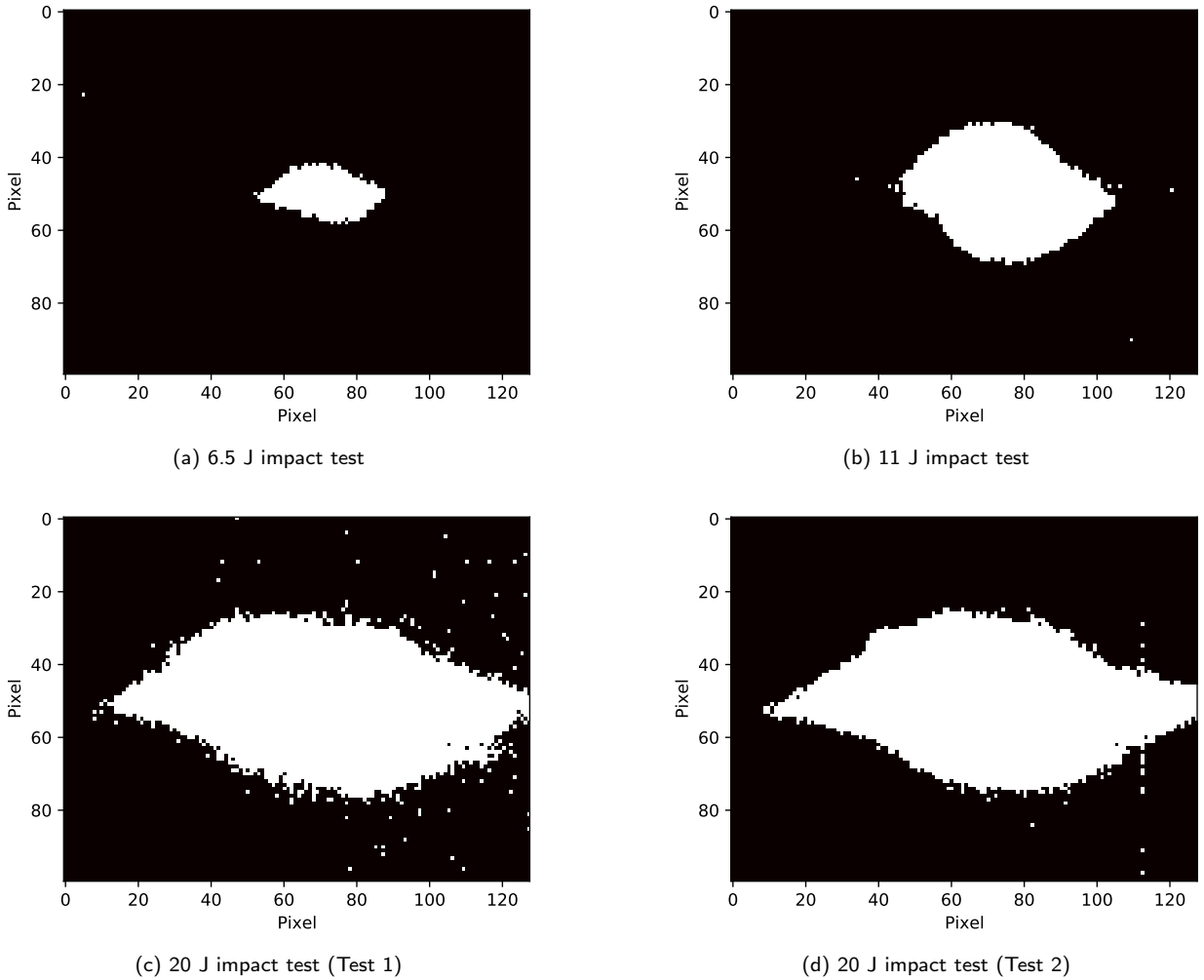


**Figure 23:** Results of the damage extension evaluation method for the different impact tests performed in this study.

## 5. *Post-mortem* damage analysis

The evolution of the temperature during impact tests has been presented in the previous section. The objective of this section is to establish some links between the thermal events and the damage mechanisms observed with other post-mortem instrumentation methods. Classical C-Scans have been performed to establish the projected damaged area. To go further and obtain volume observation of the damage mechanisms, X-Ray tomography has been performed. Finally, SEM high resolution images have highlighted the different damage mechanisms to confirm previous observations.

### 5.1. *Post-mortem* observation using SEM

After the impact event, observations were performed using a scanning electron microscope (SEM) for a sample impacted at 20J. The stitching of 0.5 mm images has been done to reconstruct a wide observation of the material's microstructure. A 0° micrograph cut is presented in Figure 24 where almost all the stacking sequence is highlighted. The black dashed line located at the midlaminar highlights the [45°/45°] interface whereas, four other colored lines represent the different interfaces. The micrograph presents an overview of the classical impact damages, where the three damage mechanisms related to matrix cracking, delamination and fibre breaks are shown in the colored square. It can be noticed that a strong interaction between the matrix cracking and the delamination is observed. Besides, for the bottom plies, a complex crack network is found. Indeed, fibre breaks in tension have occurred for the lower plies

except for the lowest 0° ply. The fibre breaks in tension is responsible for the cavities observed in the lower plies. In other words, broken fibres have been pulled out during the sample preparation for micrograph observation. This figure demonstrates the difficulty of reconstructing the damage scenario, which is very complex, using only the micrograph.

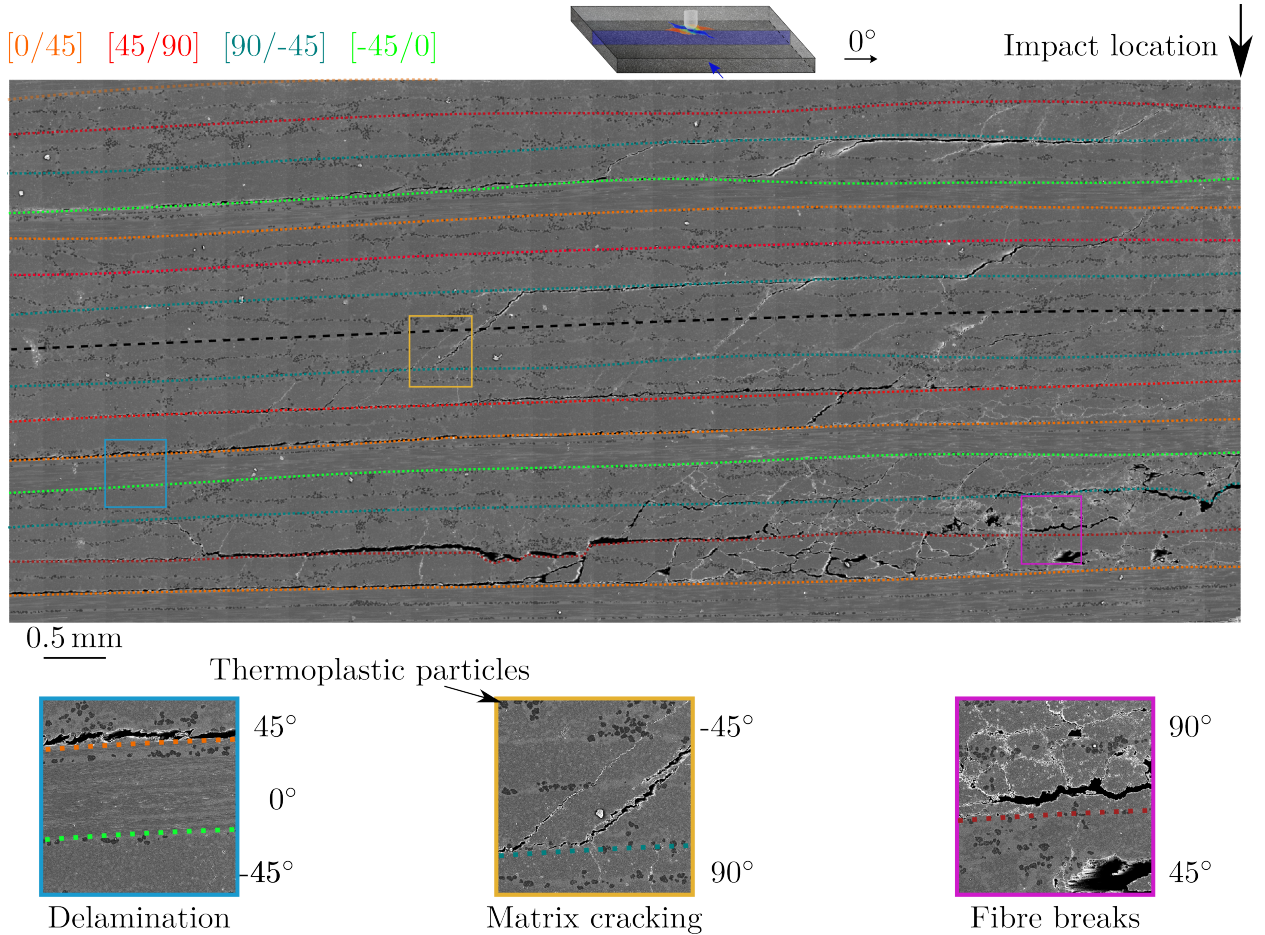


Figure 24: Micrograph observation using SEM for a sample impacted at 20J impact

## 5.2. Post-mortem ultrasonic inspection

The projected damage areas obtained by ultrasonic inspection are shown in Figure 25. This figure shows that impact damages are observed through the thickness. Moreover, it highlights the delamination evolution for the lowest interface in red, which corresponds to the highest delaminated surface at 35 J. The projected delaminated areas were estimated and are presented in Table 3. The inspection using ultrasonic scan gives an understanding of the projected damage area but is not sufficient to assess the complexity of impact damages.

## 5.3. X-ray post-mortem analysis

### 5.3.1. Image processing

After reconstruction, correction of the rotation in the three axes has been performed using the freeware ImageJ (Schneider, Rasband and Eliceiri, 2012). Once the samples were cropped and rotated, contrast enhancement was performed using the scikit-image library in python (Van der Walt, Schönberger, Nunez-Iglesias, Boulogne, Warner, Yager, Gouillart, Yu and contributors, 2014). Contrast Limited Adaptive Histogram Equalization (CLAHE) algorithm has been used first for each slice. Then, histogram matching was performed in order to get the same histogram for every slices. The reference histogram has been considered using the most damaged slice to get the best contrast. This treatment makes the segmentation of damages in the next part easier.

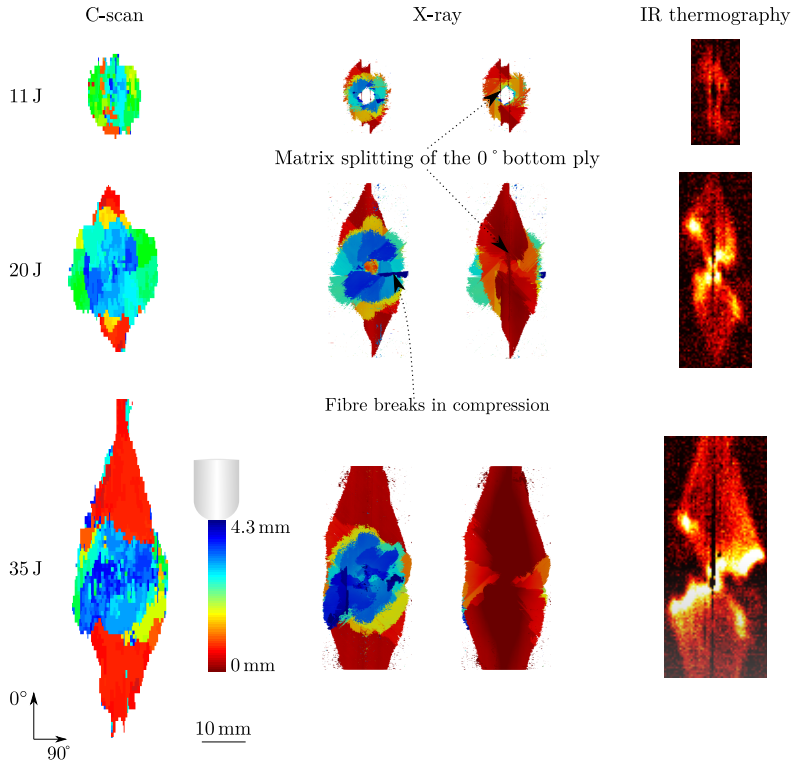


**Figure 25:** Segmentation of impact damage mechanisms obtained from C-Scan in depth, X-Ray and IR thermography at 3 different impact energy levels.

### 5.3.2. Impact damage segmentation using deep learning

#### Algorithm and parameters selection for training

After image enhancement, the segmentation was performed with the software Dragonfly ((Dragonfly 2021.1 [Linux software], 2021)). The Deep-learning toolbox integrates the TensorFlow and Keras libraries from Google (Géron (2019)). The training and inference data are performed using the deep-learning toolbox. A Conventional neural networks (CNNs) U-NET algorithm has been chosen for performing the damage segmentation. Indeed, this algorithm has been suitable to perform reliable segmentations for medical images (Ronneberger, Fischer and Brox (2015)). Relevant results have been obtained with three hidden layers for the neural network architecture. Several parameters were needed to be defined for the model training :

- patch size defines the size of 2D square patches. The image is subdivided into patches that contain local image information;
- stride-to-input ratio defines the location of the nearby patch. A stride-to-input ratio of 0.5 will overlap half of the two adjacent patches;
- Batch size contains several patches. The neural network weights are updated between two training batches;
- Epochs corresponds to the number of iterations during the training. An epoch involves the training of all batches in one iteration;

Several trials have been performed to obtain the optimal training parameters. Based on the final inference quality performed on untrained data, it has been decided to select a patch size of  $(32 \times 32)$  pixels, a stride-to-input ratio of 50% and a batch size of 2 times the patch-size.

#### Training data

The objective is to segment the different impact damage mechanisms. The main issue is that the impact damage pixel

gray value is similar to the exterior environment. Therefore, as shown in Figure 26, three labels have been defined. The first label in green is for the external environment, the second in red for the sound material, and the last in purple for the impact damages. The training data has been performed on 2D slices containing the entire thickness. It has been motivated to distinguish the three different labels easily.

For lower impact energy, the impact damages were contained within the laminate. However, for higher impact energy levels, a network between the impact damages and the external environment was observed on the top and bottom surfaces, which has made the training more complex. In consequence, 10-15 transverse images were needed to train the samples impacted at lower energies. For higher energies, the training data need 15-20 transverse images. 80% of the patches were used for training and 20% were used to evaluate the predictive capability of the trained model. After a few epochs (typically between 40 and 50), the trained model reaches fast convergence with a 98-99 % accurate score.

### *Segmentation results*

Once the model is trained, the segmentation has been performed on the untrained CT images of the composite plate. Full segmentation of the impact damages in a X-ray volume was performed in 90 minutes. Visual inspection confirmed the result's reliability. The prediction results are presented for 3 slices in different planes for the specimen impacted at 35 J in Figure 26. It can be observed that the segmentation of the three labels was performed accurately. Despite the similar grayscale levels, the impact damage is dissociated from the external environment, which confirm the reliability of the algorithm. The complex damage pattern was straightforwardly captured. It can be observed surrounded in white, that some damaged pixels were not captured by the algorithm. It could be explained by the smallest size of the damaged pixel networks which are not recognized as a crack. The projected impact damages at 20J were finally observed on the top right in Figure 26.

### **5.3.3. Impact damage investigations**

3D rendering of impact damages was performed with Paraview using a depth-coded colormap. The results are presented in Figure 25. First of all, X-ray dissociates each kind of damage mechanism (matrix cracking, delamination and fibre breaks) with high-quality damage visualization. Based on what was previously observed with infrared thermography, some assumptions regarding the damage scenario can be made using this *post-mortem* analysis. The delamination cracks propagate from the non-impacted side for the 11 J test. Before fibre breaks in tension occur, the delamination of the lowest interface [0°/45°] is clustered between the matrix cracking of the 45° ply and the outer 0° ply. However, since 20J, fibre breaks in tension occur in the lowest 45° ply. The delamination of the lowest interface [0°/45°] increases until becoming the largest delaminated area. Indeed, as observed with infrared thermography, the fibre breaks in tension of the 45° ply open the split in the 0° ply and then trigger the delamination expansion. Thanks to the matrix splitting and the largest delamination of the lowest interface [0°/45°], the bottom 0° ply is unloaded and free of fibre breaks in tension. Concerning the damage mechanisms occurring near the impacted surface, tests from 11 J shows no damage under the impactor. It is probably explained by a reinforcement of the ply strength due to local hydrostatic pressure. Fibre breaks in compression occur since 11 J for the 0° surface ply close to the impactor. For the 35 J test, fibre breaks in compression are also observed for the 45° ply just below the outer 0° surface ply.

### **5.3.4. Projected damaged area quantification**

The 3D array containing the non-zero pixels relative to the impact damage are projected on a 2D array in order to quantify the damaged area. As the pixel area is known, the damaged surface is then calculated by multiplying the total number of projected pixels by the area of one pixel.

## **6. Comparisons of projected damaged areas**

The projected damaged areas obtained from C-scan and X-ray are summarised in Table 3. They are compared to the results previously obtained from the post-treatment of the IR images summarised in Table 2. For the 35 J, the X-ray damage extension evaluation is necessarily smaller than the damage extension in the specimen, as the scanned area is smaller than the delamination extend as it can be observed in Figure 25. It can be noticed that the areas obtained with IR post-treatment are higher than areas measured from C-scan which are themselves higher than the areas computed from X-ray analysis. The differences between C-scan and X-Ray can be explained by the higher spatial resolution of the X-ray analysis. The spatial resolution of the C-scan, in this study, is 1 mm, which is 60 times greater than the resolution obtained from X-ray analysis. Regarding the comparison with the IR images post-treatment methodology

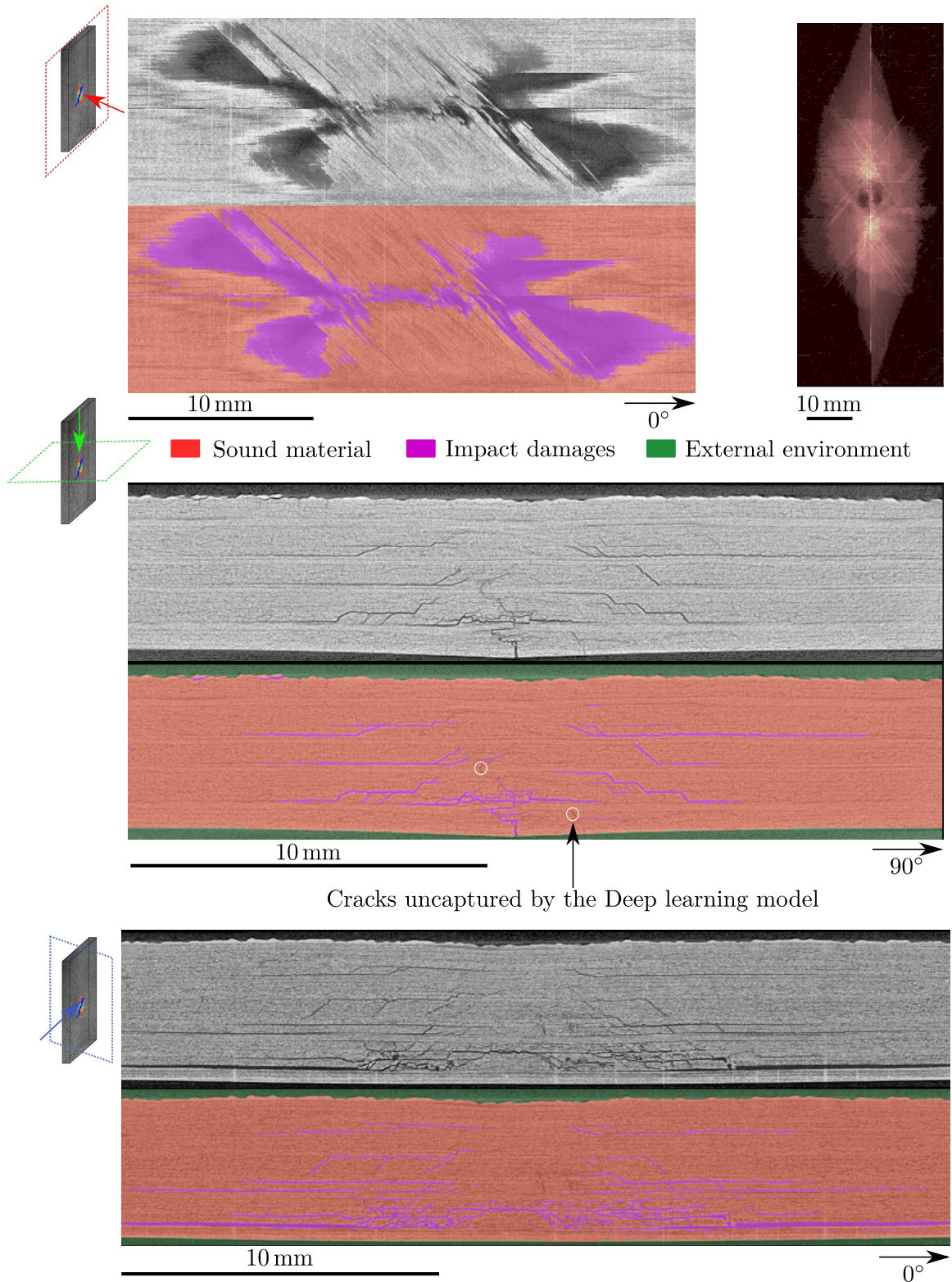


**Figure 26:** Segmentation of the different labels performed with the U-net deep learning algorithm on the untrained X-ray data. The data is obtained from the sample impacted at 20 J

used to obtain the values in Table 2, the higher values can be explained by the fact that these results necessarily include in-plane diffusion of the temperature increase due to damage, which can lead to an overestimation of the damaged area. A better understanding of these differences could probably be obtained through numerical simulations Liu, Cai, Du, Chen, Zhao and Zhang (2023).

**Table 3**

Results of the damage extension evaluation method for the different impact tests performed in this study.

Energy	6.5 J	11 J	20 J	35 J
C-scan	-	200 mm <sup>2</sup>	561 mm <sup>2</sup>	1123 mm <sup>2</sup>
X-ray	-	121.8 mm <sup>2</sup>	464.9 mm <sup>2</sup>	>845 mm <sup>2</sup>
Heated area	67.86 mm <sup>2</sup>	271.95 mm <sup>2</sup>	698.92 mm <sup>2</sup>	-

On the other hand, by comparing Figure 19 and Figure 25, it can be seen that the analysis proposed for the construction of Figure 19 clearly highlights the shape of the delamination between the last 2 plies on the non-impacted side which is depicted in dark red on the right hand side in Figure 25.

## 7. Conclusion

This study investigated the potential contributions of using high-speed infrared thermography to monitor low-speed impact tests. Tests were performed at different energy levels to demonstrate the contribution of this measurement technique to the understanding and quantification of impact damage for damage scenarios of increasing complexity. This study clearly demonstrates the ability of high-speed in-situ infrared thermography to capture the propagation of transverse and delamination crack during impact and to accurately establish the chronology of damage events as a function of the applied load. These measurements clearly open up strong perspectives for the validation of numerical models, but also increasing the dialogue between tests and simulations for this type of mechanical loading. In addition, the classical methods of post-processing of IR images available in the literature for post-test in-situ damage extension assessment have also been applied and some difficulties due to the use of high-speed infrared cameras have been highlighted. An approach based on shorter diffusion times has been proposed and implemented to overcome these difficulties and to assess the damage below the observed ply surface. Finally, these results were compared with post-mortem C-Scan and X-ray analysis. An overestimation of the damage extension area with IR post-treatment methods, based on images taken a long time after the impact tests, was observed and explained.

## Acknowledgements

The authors would like to thank Fabrice Concourdeau, Dominique Martini and Vincent Jacques from Dassault Aviation for valuable discussions about impact on composite materials. We also thank Dassault Aviation and DGAC for their financial support. The authors also gratefully acknowledge the Hauts-de-France Region for funding equipment that contributed to this research work. Finally the authors would like to thank Jean-Claude Daux and Patrick Lapeyronnie for the modification of the impact machine in order to be able to perform this study.

## Data Availability

The raw/processed data required to reproduce these findings cannot be shared at this time due to technical or time limitations.

## References

- Abrate, S., 1998. Impact on Composite Structures. Cambridge University Press. doi:10.1017/CB09780511574504.
- Allix, O., Blanchard, L., 2006. Mesomodeling of delamination: towards industrial applications. Composites Science and Technology 66, 731–744.
- Aymerich, F., Meili, S., 2000. Ultrasonic evaluation of matrix damage in impacted composite laminates. Composites Part B: Engineering 31, 1–6.
- Battams, G., Dulieu-Barton, J., 2016. Data-rich characterisation of damage propagation in composite materials. Composites Part A: Applied Science and Manufacturing 91, 420–435.

- Berthe, J., Ragonet, M., 2018. Passive infrared thermography measurement of transverse cracking evolution in cross-ply laminates. *Strain* 54, e12293.
- Boccardi, S., Carlomagno, G., Simeoli, G., Russo, P., Meola, C., 2016. Evaluation of impact-affected areas of glass fibre thermoplastic composites from thermographic images. *Measurement Science and Technology* 27.
- Bouvet, C., Castanié, B., Bizeul, M., Barrau, J.J., 2009. Low velocity impact modelling in laminate composite panels with discrete interface elements. *International Journal of Solids and Structures* 46, 2809–2821.
- Bouvet, C., Rivallant, S., 2023. 2 - damage tolerance of composite structures under low-velocity impact, in: Silberschmidt, V. (Ed.), *Dynamic Deformation, Damage and Fracture in Composite Materials and Structures (Second Edition)*. second edition ed.. Woodhead Publishing. Woodhead Publishing Series in Composites Science and Engineering, pp. 3–28. URL: <https://www.sciencedirect.com/science/article/pii/B9780128239797000028>, doi:<https://doi.org/10.1016/B978-0-12-823979-7.00002-8>.
- Bull, D., Helfen, L., Sinclair, I., Spearing, S., Baumbach, T., 2013. A comparison of multi-scale 3d x-ray tomographic inspection techniques for assessing carbon fibre composite impact damage. *Composites Science and Technology* 75, 55–61.
- Cantwell, W., Morton, J., 1989. Geometrical effects in the low velocity impact response of cfrp. *Composite Structures* 12, 39–59.
- Chaibi, S., 2022. Prédiction des endommagements induits par un impact basse vitesse/basse énergie au sein de matériaux composites stratifiés carbone-époxy de dernière génération. Ph.D. thesis. Toulouse, ISAE.
- Choi, H.Y., Downs, R., Chang, F.K., 1991. A new approach toward understanding damage mechanisms and mechanics of laminated composites due to low-velocity impact: Part i—experiments. *Journal of composite materials* 25, 992–1011.
- Cuynet, A., Scida, D., Roux, É., Toussaint, F., Ayad, R., Lagache, M., 2018. Damage characterisation of flax fibre fabric reinforced epoxy composites during low velocity impacts using high-speed imaging and stereo image correlation. *Composite Structures* 202, 1186–1194.
- Davies, G., Olsson, R., 2004. Impact on composite structures. *The Aeronautical Journal* 108, 541–563.
- De Moura, M., Gonçalves, J., 2004. Modelling the interaction between matrix cracking and delamination in carbon–epoxy laminates under low velocity impact. *Composites Science and Technology* 64, 1021–1027.
- Dragonfly 2021.1 [Linux software], 2021. Object Research Systems (ORS) Inc, Montreal, Canada; software available at <http://www.theobjects.com/dragonfly>.
- Ellison, A.C., 2020. Segmentation of X-ray CT and Ultrasonic Scans of Impacted Composite Structures for Damage State Interpretation and Model Generation. Ph.D. thesis.
- Flores, M., Mollenhauer, D., Runatunga, V., Beberniss, T., Rapping, D., Pankow, M., 2017. High-speed 3d digital image correlation of low-velocity impacts on composite plates. *Composites Part B: Engineering* 131, 153–164.
- Géron, A., 2019. Hands-on machine learning with Scikit-Learn, Keras, and TensorFlow: Concepts, tools, and techniques to build intelligent systems. " O'Reilly Media, Inc."
- Hawyes, V., Curtis, P., Soutis, C., 2001. Effect of impact damage on the compressive response of composite laminates. *Composites Part A: Applied Science and Manufacturing* 32, 1263–1270. URL: <https://www.sciencedirect.com/science/article/pii/S1359835X01000720>, doi:[https://doi.org/10.1016/S1359-835X\(01\)00072-0](https://doi.org/10.1016/S1359-835X(01)00072-0).
- Hempe, D.W., 2010. AC 20-107B ADVISORY CIRCULAR COMPOSITE AIRCRAFT STRUCTURE. Technical Report. 0-Advisory U.S. Department of Transportation Circular Federal Aviation Administration.
- Johnston, J.P., Pereira, J.M., Ruggeri, C.R., Roberts, G.D., 2018. High-speed infrared thermal imaging during ballistic impact of triaxially braided composites. *Journal of Composite Materials* 52, 3549–3562.
- Kwon, Y.S., Sankar, B.V., 1993. Indentation-flexure and low-velocity impact damage in graphite epoxy laminates. *Journal of Composites, Technology and Research* 15, 101–111.
- Li, S., Reid, S.R., Zou, Z., 2006. Modelling damage of multiple delaminations and transverse matrix cracking in laminated composites due to low velocity lateral impact. *Composites Science and Technology* 66, 827–836.
- Liu, P., Cai, Y., Du, C., Chen, Y., Zhao, Z., Zhang, C., 2023. An elastoplastic mechanical-thermal model for temperature rise simulation of two-dimensional triaxially braided composites under quasi-static loads. *Composite Structures* 306, 116559.
- Lopes, C., Camanho, P., Gürdal, Z., Maimí, P., González, E., 2009. Low-velocity impact damage on dispersed stacking sequence laminates. part ii: Numerical simulations. *Composites Science and Technology* 69, 937–947.
- Maierhofer, C., Krankenhagen, R., Röllig, M., 2019. Application of thermographic testing for the characterization of impact damage during and after impact load. *Composites Part B: Engineering* 173.
- Meola, C., Boccardi, S., Carlomagno, G.M., 2018. A quantitative approach to retrieve delamination extension from thermal images recorded during impact tests. *NDT & E International* 100, 142–152.
- Meola, C., Carlomagno, G.M., 2009. Infrared thermography of impact-driven thermal effects. *Applied Physics A* 96, 759–762.
- Meola, C., Carlomagno, G.M., 2010. Impact damage in gfrp: new insights with infrared thermography. *Composites Part A: Applied Science and Manufacturing* 41, 1839–1847.
- Namala, K.K., Mahajan, P., Bhatnagar, N., 2014. Digital image correlation of low-velocity impact on a glass/epoxy composite. *International Journal for Computational Methods in Engineering Science and Mechanics* 15, 203–217.
- Olsson, R., 2000. Mass criterion for wave controlled impact response of composite plates. *Composites Part A: Applied Science and Manufacturing* 31, 879–887. URL: <https://www.sciencedirect.com/science/article/pii/S1359835X00000208>, doi:[https://doi.org/10.1016/S1359-835X\(00\)00020-8](https://doi.org/10.1016/S1359-835X(00)00020-8).
- Pan, Z., Wu, Z., Xiong, J., 2019. High-speed infrared imaging and mesostructural analysis of localized temperature rise in damage and failure behavior of 3-d braided carbon/epoxy composite subjected to high strain-rate compression. *Polymer Testing* 80.
- Pan, Z., Wu, Z., Xiong, J., 2020. Localized temperature rise as a novel indication in damage and failure behavior of biaxial non-crimp fabric reinforced polymer composite subjected to impulsive compression. *Aerospace Science and Technology* 103.
- Portemont, G., Berthe, J., Deudon, A., Irisarri, F.X., 2018. Static and dynamic bearing failure of carbon/epoxy composite joints. *Composite Structures* 204, 131–141.

- Ronneberger, O., Fischer, P., Brox, T., 2015. U-net: Convolutional networks for biomedical image segmentation, in: International Conference on Medical image computing and computer-assisted intervention, Springer. pp. 234–241.
- Schneider, C.A., Rasband, W.S., Eliceiri, K.W., 2012. NIH Image to ImageJ: 25 years of image analysis. *Nature Methods* 9, 671–675. URL: <https://doi.org/10.1038/nmeth.2089>, doi:10.1038/nmeth.2089.
- Topac, O.T., Gozluklu, B., Gurses, E., Coker, D., 2017. Experimental and computational study of the damage process in cfrp composite beams under low-velocity impact. *Composites Part A: Applied Science and Manufacturing* 92, 167–182.
- Trousset, E., 2013. Prévission des dommages d'impact basse vitesse et basse énergie dans les composites à matrice organique stratifiés. Ph.D. thesis. Ecole nationale supérieure d'arts et métiers-ENSAM.
- Van der Walt, S., Schönberger, J.L., Nunez-Iglesias, J., Boulogne, F., Warner, J.D., Yager, N., Gouillart, E., Yu, T., contributors, t.s.i., 2014. scikit-image: image processing in Python. *PeerJ* 2, e453. URL: <https://doi.org/10.7717/peerj.453>, doi:10.7717/peerj.453.
- Wronkowicz-Katunin, A., Katunin, A., Dragan, K., 2019. Reconstruction of barely visible impact damage in composite structures based on non-destructive evaluation results. *Sensors* 19. URL: <https://www.mdpi.com/1424-8220/19/21/4629>, doi:10.3390/s19214629.